

# Thermoelectric Properties of ITO and SnSe Nanowires and Sb<sub>2</sub>Se<sub>3</sub> Hexagonal Nanotubes

by  
José Alberto Hernández Pérez

A dissertation submitted in partial fulfillment of the requirements for the degree of

Doctor of Philosophy  
in  
Chemical Physics

UNIVERSITY OF PUERTO RICO  
RIO PIEDRAS CAMPUS

August 2018

Approved by:

---

Luis F Fonseca, Ph.D.  
Thesis Advisor

---

Date

---

Gerardo Morell, Ph.D.  
Thesis Committee Member

---

Date

---

Carlos Cabrera, Ph.D.  
Thesis Committee Member

---

Date

Copyright © August 2018  
by  
José Alberto Hernández Pérez

# Thermoelectric Properties of ITO and SnSe Nanowires and Sb<sub>2</sub>Se<sub>3</sub> Hexagonal Nanotubes

José Alberto Hernández Pérez

Doctor of Philosophy in Chemical Physics

University of Puerto Rico at Rio Piedras Campus

Dr. Luis F Fonseca, Faculty Advisor, Department of Physics

## (ABSTRACT)

The synthesis of multifunctional nanomaterials has received great attention in the last years due to the possibility of integrating multiple functionalities into individual building blocks to enable the fabrication of novel and powerful devices. At the same time, power dissipation is an increasingly important challenge in actual industry, specially with highly miniaturized devices. In this way, thermoelectric materials have been the subject of great attention due to the possibility of interchanging thermal gradients and electric fields, specially in the retrieval of waste heat. This work is a study of the thermoelectric and transport properties of single Indium Tin Oxide (ITO) nanowires with a thermal tolerance of 1300 °C, Tin Selenide (SnSe) nanowires with diameters in the range between 110 nm and 1150 nm, and Antimony Selenide (Sb<sub>2</sub>Se<sub>3</sub>) hexagonal nanotubes. Their electrical and thermal conductivities, and the Seebeck coefficient were measured in each individual nanowire/nanotube using specialized suspended micro-resistance thermometry devices in the  $\sim 120 - 370$  K temperature range. The measured properties were correlated to electronic and lattice information obtained with model simulations and phonon's dynamics. Conclusions are drawn in each case about the applicability of these materials in energy production and waste heat recovery, the performance of the

nanoscale structures as compared with bulk samples, and their advantages and disadvantages. The work about ITO nanowires brings new data about their thermal tolerance and their potential as thermoelectric converters working in harsh environments. The work on SnSe nanowires offers the first study of the thermoelectrical properties of this material in nanowire shape and brings appealing unexpected results about the possible size dependence of their lattice thermal conductivity. The work about Sb<sub>2</sub>Se<sub>3</sub> nanotubes shows promising thermoelectric figures of merit and the first comprehensive study of the thermoelectric properties of such structures.



# Dedication

---

---

*Dedicated to my children, Pilar Melissa, Sofia Elena and Luis Andres, my source of  
motivation and inspiration.*

*This page has been intentionally left blank.*

# Acknowledgments

---

---

To professor Luis Fonseca for allowing me to develop my skills in his laboratory and his constant support, without his help this work would never be done. I am thankful to the members of my PhD advisory committee who attended my defense and made invaluable comments: Professor Carlos Cabrera and Professor Gerardo Morell.

Dr. Angel Ruiz for the collaboration with the theoretical calculations.

I would like to mention many friends around the campus who have helped me: Dr. Luis Valentin, Dr. Jennifer Carpena, Oscar Resto, Jorge Falcon, Soraya Flores, Leandro Paulino, Samuel Martinez, Álvaro Instan, Danilo Barrionuevo, Yamile Rosas, Valerio Dorvilien and many others.

*This page has been intentionally left blank.*

# Table of Contents

<b>List of Publications</b>	<b>x</b>
<b>List of Presentations</b>	<b>xi</b>
<b>List of Figures</b>	<b>xii</b>
<b>List of Tables</b>	<b>xv</b>
<b>List of Symbols</b>	<b>xvi</b>
<b>Chapter 1. Introduction</b>	<b>9</b>
1.1 Motivation . . . . .	9
1.2 Thermoelectric Effects . . . . .	10
1.2.1 Seebeck Effect . . . . .	10
1.2.2 Peltier Effect . . . . .	12
1.2.3 Thomson Effect . . . . .	13
1.3 Thermoelectric Effect in a Semiconductor . . . . .	13
1.4 The Figure of Merit . . . . .	16
1.5 Wiedeman - Franz Law . . . . .	18
1.6 Modified Debye-Callaway Model . . . . .	19
1.7 VASP and BoltzTraP Packages - General Aspects . . . . .	20
1.7.1 VASP . . . . .	20
1.7.2 BoltzTraP . . . . .	21
1.8 References . . . . .	23
<b>Chapter 2. Synthesis, Characterization Techniques and Experimental Setup</b>	<b>26</b>
2.1 Synthesis of Nanowires: Chemical Vapor Deposition (CVD) via Vapor Liquid Solid (VLS) . . . . .	26
2.2 Experimental Characterization Techniques . . . . .	28
2.2.1 X-ray Diffraction (XRD) . . . . .	28
2.2.2 Scanning Electron Microscopy (SEM) . . . . .	30

2.2.3	Transmission Electron Microscopy (TEM)	31
2.2.4	Focused Ion Beam (FIB)	33
2.3	Experimental Thermoelectric Device and Setup	35
2.3.1	Thermoelectric Device	35
2.3.2	Experimental Setup	36
2.3.3	Thermoelectric and thermal conductance measurements	38
2.4	References	44
<b>Chapter 3. Thermoelectric Properties and Thermal Tolerance of Indium Tin Oxide Nanowires</b>		<b>45</b>
3.1	Introduction	45
3.2	Synthesis and Characterization	47
3.3	Thermoelectric Measurements and Discussion	50
3.4	Conclusions	57
3.5	References	59
<b>Chapter 4. Thermoelectric Properties of SnSe Nanowires with different diameters</b>		<b>67</b>
4.1	Introduction	67
4.2	Experimental Results, calculations and Discussion	68
4.3	Summary	84
4.4	References	87
<b>Chapter 5. Thermoelectric Properties of Sb<sub>2</sub>Se<sub>3</sub> Hexagonal Nanotubes</b>		<b>90</b>
5.1	Introduction	90
5.2	Experimental Results and Discussion	91
5.3	Summary	97
5.4	References	98
<b>Chapter 6. Concluding Remarks and Future Recommendations</b>		<b>101</b>
6.1	Conclusions	101
6.2	Future Recommendations	103

# List of Publications

---

---

## Thesis Related Publications

- Jose A. Hernandez, Jennifer Carpena-Nunez, Luis F. Fonseca, Michael Pettes, Miguel J Yacamán, and Alfredo Benitez. Thermoelectric Properties and Thermal Tolerance of Indium Tin Oxide Nanowires. *Nanotechnology* 29 (2018) 364001.
- Jose A. Hernandez, Angel Ruiz, Luis F. Fonseca, Michael T. Pettes, Miguel Jose Yacamán and Alfredo Benitez. Thermoelectric properties of SnSe nanowires with different diameters. *Scientific Reports* 2018.
- Manuscript under edition: Jose A. Hernandez, Luis F. Fonseca, Michael Pettes, Miguel Jose Yacamán and Arturo Ponce. Thermoelectric Properties of Antimony Selenide Hexagonal Nanotubes.

## Collaboration Publications

- Yang, Dachi, Jose A. Hernandez, Ram S. Katiyar, and Luis F. Fonseca. Surface morphology-controlled fabrication of  $\text{Na}_2\text{WO}_4$  films with high structural stability. *Chemical Physics Letters* 653 (2016) 73-77.
- Manuscript Submitted: Angel Ruiz, Jose A Hernandez, Luis Fonseca, Miguel Yacamán, Eduardo Ortega, and Arturo Ponce. High Curie Temperature CoSi nanowires by Mn<sup>-</sup>doping. **J. Appl. Phys.**
- Manuscript Submitted: Ruiz, Angel; Hernandez, Jose; Fonseca, Luis; Yacaman, Miguel; Ortega, Eduardo; Ponce-Pedraza, Arturo. Single nanowire measurements of room temperature ferromagnetism in FeSi nanowires and the effects of Mn-doping. **Nanotechnology**

## Educational Publications

- José A. Hernández-Pérez y Carlos Torrech. Enseñanza de las Matemáticas Incorporando las Ciencias en el Aula y Las Competencias Matemáticas. *Revisita el Sol. Departamento de Educación de Puerto Rico* 2015.
- Khaled Habiba, José A. Hernández-Pérez; Anibal A. Hernández Vega; Adriana Rivera, Kennett Rivero; Carlos J. Valle Díaz y Liz M. Díaz-Vázquez. "La Nanotecnología Llega a la Exhibición Educativa Oceánica". *Revisita el Sol. Departamento de Educación de Puerto Rico* 2015.

# List of Presentations

---

---

- VI Escuela NanoAndes 2016: Propiedades Termoeléctricas de Nano-hilos de Telurio de Estaño José A. Hernández-Pérez and Luis F. Fonseca. Nov 7-12, Cali, Colombia.
- IFN EPSCoR Annual Meeting - 2016. Thermoelectric and Transport Properties of SnSe and SnTe Nanowires Jose A. Hernández-Pérez, Angel Ruiz-Reyes and Luis F. Fonseca. Caguas PR, USA.
- WWN & WOFE Workshop 2015: Thermoelectric Properties of a Single Tin Selenide Nanowire José A. Hernández-Pérez, Angel Ruiz and Luis F. Fonseca. San Juan PR, USA.
- MS&T 2015: TEM and MFM Studies of Mn<sup>+</sup> Ion Implanted CoSi and FeSi Nanowires. José A. Hernández-Pérez, Angel Ruiz and Luis F. Fonseca. Columbus OH, USA.
- PRLAMP: Nature and Technology in Parallel: An interdisciplinary module of Science-Technology-Engineering-Art-Mathematics (STEAM) for 8th-12th grade students. Carlos J. Valle-Díaz, Jose A. Hernández-Pérez, Eliana Bendezú-Portela, Carlos A. Torrech-Prieto, Elvia Meléndez-Ackerman, Gladys Dávila-Hernández, Liz Díaz-Vázquez. Caguas PR, USA.
- MRS 2014: Poster: Thermoelectric properties and Thermal Tolerance of Indium Tin Oxide Nanowires. José A. Hernández-Pérez, Jennifer Carpena-Nunez, Luis Valentín and Luis F. Fonseca. San Francisco CA, USA.
- IFN EPSCoR Annual Meeting - 2014: Thermoelectric properties of Indium Tin Oxide Nanowires for Photovoltaic Applications. José A. Hernández-Pérez, Jennifer Carpena-Nunez, Luis Valentín and Luis F. Fonseca. Caguas PR, USA.
- IFN EPSCoR Annual Meeting - 2014: Silicides Nanowires for Spintronics Applications. José A. Hernández-Pérez, Angel Ruiz and Luis F. Fonseca. Caguas PR, USA.



# List of Figures

Figure 1.1	Illustration of the temperature gradient effect over the majority charge density in a material. . . . .	11
Figure 1.2	Illustration of the (a) Seebeck Effect and (b) Peltier Effect. . . . .	12
Figure 1.3	Illustration of Two contacts with the same electrochemical potential $\mu$ at different temperatures.. . . .	14
Figure 2.1	CVD Schematic Setup Representation. . . . .	27
Figure 2.2	Schematic representation of VLS mechanism for growth ITO nanowires..	27
Figure 2.3	Illustration of (a) incident and scattered plane wave into a interplanar $d$ (b) Crystal parameters for Cubic, Orthorhombic and Hexagonal lattice. .	29
Figure 2.4	Illustration of different signals from a typical electron beam interaction with a bulk sample in a SEM.. . . .	31
Figure 2.5	Signals generated when a high-energy beam of electrons interacts with a thin specimen. Most of these signals can be detected in different types of TEM.. . . .	32
Figure 2.6	Focused Ion Beam diagram representation - the organometallic is used to deposit contacts. . . . .	34
Figure 2.7	Different magnification of micro-device into a chip carrier for a SnSe measured sample. . . . .	35
Figure 2.8	Experimental thermal resistance diagram and schematic setup for thermal resistance or conductance measurements of individual Nanowire. . .	37
Figure 2.9	(a) Measured total heat $Q_{Total} = Q_h + Q_L$ plotted as function of $T_h + T_s$ for sample 2 of $Sb_2Te_3$ nanobelt, the slope give us the total thermal conductance $G_B$ . (b) The obtained $\Delta T_s$ as a function of $\Delta T_h - \Delta T_s$ , the slope yields $G_m/GB$ . (c) and (d) are the change in temperature of the heating membrane $\Delta T_h$ and sensing membrane $\Delta T_s$ as a function of ramped $I_{dc}$ for 3 cycles. . . . .	39
Figure 2.10	Schematic diagram of the nanowire suspended between two suspended membranes indicating various length segments for the fin model analysis..	41
Figure 3.1	SEM images for ITO nanowires (a), (b) as-synthesized, (c), (d) After 1300°C annealing and (e), (f) After 1400°C annealing.. . . .	47

Figure 3.2	(a) SEM image, insert: SAED patten for sample before annealing. (b) SEM-EDS mappings (c) XRD patter for sample on substrate before and after 1300 °C annealing.. . . . .	48
Figure 3.3	SEM images and EDS mapping for No annealing measures samples..	50
Figure 3.4	SEM images and EDS mapping for measured samples with annealing..	51
Figure 3.5	SEM images for a one single ITO nanowire onto specialized device..	52
Figure 3.6	(a) Measured Seebeck coefficient $S$ , (b) Thermal Conductivity ( $\kappa$ ), electrical conductivity ( $\sigma$ ) and (d) $ZT$ as a function of Temperature of ITO nanowires.. . . . .	53
Figure 3.7	(a) Electron thermal conductivity. (b) Lattice thermal conductivity as function of temperature. The continue lines are the model fittings.. . . .	55
Figure 4.1	Summary art concept of SnSe study. . . . .	67
Figure 4.2	(a) SEM image of the as-grown SnSe nanowires. (b) HRTEM and SAED for a measured SnSe NW (1.15 $\mu\text{m}$ ). (c) XRD pattern, (* corresponds to the sapphire substrate). (d) SEM EDS mapping for a measured SnSe nanowire (480 nm).. . . . .	69
Figure 4.3	SEM - EDS spectra for 3 SnSe nanowire samples. The inset shows the atomic ratio for Sn and Se.. . . . .	71
Figure 4.4	SEM images of SnSe nanowires aligned on specialized micro devices for diameters between 1.15 $\mu\text{m}$ to 130 nm.. . . . .	72
Figure 4.5	From left to right, optical image of the micro-thermometry device wired to a chip carrier, followed by low and high magnification SEM images of a 130 nm nanowire transferred onto the micro-device.. . . . .	73
Figure 4.6	(a) Measured Seebeck coefficient $S$ , (b) thermal conductivity $\kappa$ , (c) electrical conductivity $\sigma$ and (d) $ZT$ of SnSe nanowires with different diameters as a function of temperature.. . . . .	74
Figure 4.7	SEM images of the growth nanowire on substrate. The cross section suggests rounded shape.. . . . .	76
Figure 4.8	(a) Lattice thermal conductivity in comparison with calculated accumulated thermal conductivity data of Guo et. al. [14] in a, b and c directions and (b) figure of merit $ZT$ at 290 K for different diameters.. . . . .	78
Figure 4.9	(a) Crystal structure of the Pnma phase of SnSe. The primitive cell is shown as a black line. Gray larger balls represent Sn atoms and green smaller balls are Se atoms. (b) The calculated band structure and (c) the total density of states.. . . . .	79

Figure 4.10	The calculated thermoelectric properties of SnSe. (a) Seebeck coefficient as a function of the chemical potential ( $\mu - E_{VBM}$ ), the energy position of the band edges ( $E_{VBM}$ and $E_{CBM}$ ) is identified by vertical dotted lines. (b) The calculated temperature dependences of the chemical potential ( $\mu - E_{VBM}$ ). (c) The calculated electron ( $\kappa_e$ ) and (d) lattice ( $\kappa_{ph}$ ) thermal conductivities contributions. Calculated $\kappa_{ph}$ from Guo et. al. [14] is shown in figure (d) with continuous lines in $a$ , $b$ and $c$ crystal directions.. . . . .	80
Figure 4.11	The measured lattice thermal conductivities ( $\kappa_{ph}$ ) for each nanowire. The calculated $\kappa_{ph}$ for two diameters ( $L_1$ and $L_2$ ) are shown with continuous lines.. . . . .	83
Figure 4.12	(a) Supercell Crystal structure of the low temperature Pnma phase SnSe with 18 layers. Gray balls are Sn atoms and green are Se atoms. (b) Calculated Density of States per layer as a function of the chemical potential for modeled nanowire with 5 nm in diameter (c) is the same as (b) with different scales.. . . . .	85
Figure 5.1	SEM images of $Sb_2Se_3$ nanotubes on substrate (a) and (b) shows a different magnification of as grown HNT. (c) and (d) show the hexagonal nanotube morphology of the samples.. . . . .	92
Figure 5.2	a) SEM image of $Sb_2Se_3$ hexagonal as grown nanotubes on the substrate. (b) XRD pattern of as grown material on the substrate. (c) SEM image and SEM-EDS mapping of Sb and Se signals. (d) HRTEM image, insert: SAED.. . . . .	93
Figure 5.3	SEM images of measured $Sb_2Se_3$ hexagonal nanotubes aligned on specialized suspended micro devices, (a) and (b) different magnification images of sample 1. (c) SEM image of sample 2 and (d) SEM-EDS spectra and atomic percentages of elements found in the measured samples.. . . . .	94
Figure 5.4	(a) Measured Seebeck coefficient $S$ for the two samples as compared with Bulk calculations [14]. (b) total thermal conductivity $\kappa$ of the HNT with the error bars. (c) Electrical conductivity of the measured samples. (d) calculated figure of merit $ZT$ for the samples as a function of temperature.. . . . .	95
Figure 5.5	Calculate lattice thermal conductivity for the measured samples as a function of temperature.. . . . .	96

# List of Tables

---

---

Table 3.1	Summary of atomic percent concentration approximation of measured ITO nanowires.. . . . .	49
Table 3.2	Values of impurities (A) and boundary (D) parameters used in the modified Debye-Callaway model given by equation 3.1.. . . . .	57

# List of Symbols

---

---

AFM	Atomic Force Microscopy
cm	Centimeter
°C	Degree Celsius
CVD	Chemical Vapor Deposition
DFT	Density Functional Theory
EDS	Energy Dispersion Spectroscopy
EELS	Electron Energy Loss Spectroscopy
eV	Electron Volt
FCC	Faced Centered Cubic
FE	Field Emission
$h$	Planck constant
HRSEM	High Resolution Scanning Electron Microscopy
K	Kelvin
KeV	Kilo Electron Volt
mm	Milimeter
NW	Nanowire
$\lambda$	Wavelength
$\Omega \times m$	Ohms per meter
PRT	Platinum Resistance Thermometer
RIE	Reactive Ion Etching
$S m^{-1}$	Siemens/meter
SAED	Selective Area Electron Diffraction

---

SEM	Scanning Electron Microscopy
STEM	Scanning Transmission Electron Microscopy
Si	Silicon
SiN <sub>x</sub>	Silicon Nitride
TE	Thermoelectric
TEM	Transmission Electron Microscopy
TI	Topological Insulator
$\mu\text{m}$	Micrometer
V	Volts
$\text{W K}^{-1}\text{m}^{-1}$	Watt/Meter Kelvin
VLS	Vapor Liquid Solid
XRD	X-ray Diffraction
VASP	The Vienna Ab initio Simulation Package
ZT	Thermoelectric Figure of Merit

# Chapter 1

## Introduction

---

### 1.1 Motivation

About 66% of the energy used in power conversion processes is ejected into the environment. Finding proper materials and procedures to reuse this waste energy could play an important role in the future of energy conversion systems at all scales, specially focusing attention on technologies that can reduce ozone depletion, greenhouse gas emissions and fossil fuel usage. In order to decrease this percent of waste energy, thermoelectric materials have recently increased their worldwide acceptance due to the capacity to directly interconvert heat and electricity without moving parts. Thermoelectric materials are now the focus of research as promising building blocks of new devices for future applications in power generation and heat exchange. For example, many researches are looking for materials with relative good thermoelectric properties and good thermal tolerance  $\sim 1000$  °C.

The main focus in thermoelectricity is to find a material (or a materials set) that can increase the conversion efficiency in order to be competitive with actual technology in

generation power and heat exchange systems [1]. The conversion efficiency in thermoelectrics is governed by the so-called figure of merit ( $ZT$ ), defined as  $ZT = \frac{S^2\sigma T}{\kappa}$ , where  $S$  is the Seebeck coefficient,  $\sigma$  is the electrical conductivity,  $T$  is the absolute temperature and  $\kappa$  is the total thermal conductivity. The thermal conductivity has electronic ( $\kappa_e$ ) and lattice ( $\kappa_L$ ) contributions. To increase the conversion efficiency, the approach in this work is to synthesize materials with high Seebeck coefficients but with sizes in the nanoscale, such as nanowires, nanobelts, and nanotubes to enhance the surface-to-volume ratio, thus taking advantage of the scattering of phonons at the surface boundaries to reduce the thermal conductivity [2-4] without reducing the electrical conductivity.

## 1.2 Thermoelectric Effects

Thermoelectric devices are mainly-based on the following physical effects: Seebeck effect, Peltier effect and Thomson effect [5]. The next is a briefly introduction on each one.

### 1.2.1 Seebeck Effect

When a material is in a temperature gradient, a voltage difference  $\Delta V$  proportional to the temperature difference  $\Delta T$  is created. The ratio of the voltage to the temperature difference is related to an intrinsic property of the material. Historically this property has been known as the thermopower and here named as the Seebeck coefficient  $S$ , and



defined by:

$$S = - \left( \frac{dV}{dT} \right)_T \quad (1.1)$$

The Seebeck coefficient is the electric potential gradient produced per unit temperature gradient. The sign of the Seebeck coefficient is determined by the direction of current flow. As the temperature of the heat source  $T_1$  is greater than cool side  $T_2$ , if the electron current is flowing to the right then the Seebeck coefficient is negative, and if the positive charge current is flowing to the right, the Seebeck coefficient is positive, see figure 1.1.

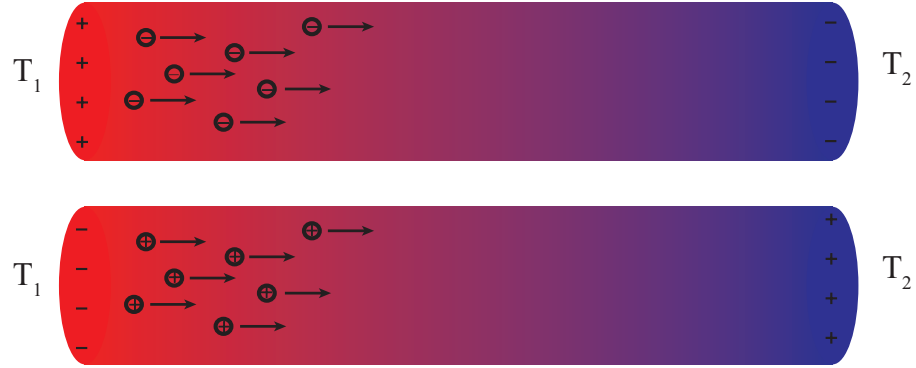


Figure 1.1: Illustration of the temperature gradient effect over the majority charge density in a material

This measurement allows one to characterize a material as *n*-type or *p*-type, meaning if the electrical current is transported by negative or positive charges, respectively. The Seebeck coefficient is temperature dependent and is obtained experimentally if the voltage between terminals (cool and hot side) and the temperatures of each one are known. The experimental data reported here, was obtained using a four-point configuration in order to take into account the electrical and thermal contacts resistances. Figure 1.2 (a) shows when two different materials *n*- and *p*-type are joined, this configuration increases the

voltage output, ideal for thermocouple and thermoelectric device applications.

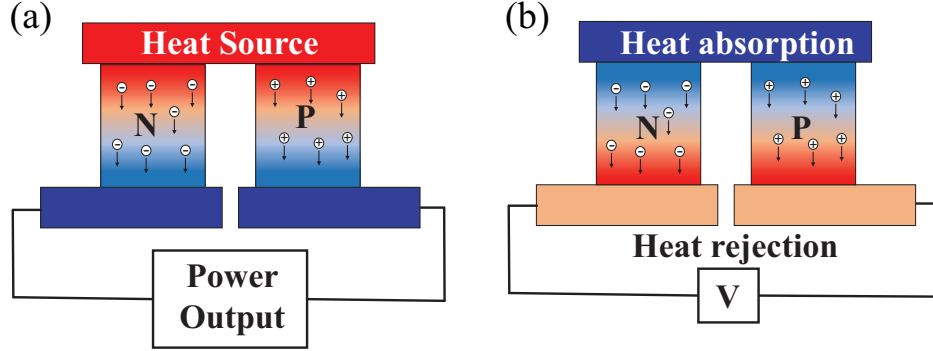


Figure 1.2: Illustration of the (a) Seebeck Effect and (b) Peltier Effect

### 1.2.2 Peltier Effect

The Peltier effect is the inverse of the Seebeck effect, if a voltage is applied across the junction between two different materials, depending on the direction of the current  $I$ , a generation or absorption of heat  $Q$  at the two junctions is observed, see figure 1.2(b) shows an illustration. The Peltier coefficient is defined by the ratio of the current ( $I$ ) to the rate of heating ( $Q$ ):

$$\pi = \frac{I}{Q} \quad (1.2)$$

The sign of  $\pi$  of the direction of current flow and which junction is heated and which is cooled.

### 1.2.3 Thomson Effect

The Thomson effect describes a electric current generated in a single conductor when a small temperature gradient is applied. This relationship is described by the equation:

$$q = \beta I \delta T \quad (1.3)$$

where  $q$  is the rate of heating,  $I$  is the electric current intensity,  $\delta T$  is the change in temperature and  $\beta$  is the Thomson coefficient. This relationship is a good approximation for small  $\delta T$ . Finally all of these coefficients are related by the Kelvin relations:

$$\pi_{ab} = T S_{ab} \quad (1.4)$$

$$\frac{dS_{ab}}{dT} = \frac{\beta_a - \beta_b}{T} \quad (1.5)$$

## 1.3 Thermoelectric Effect in a Semiconductor

The next is a brief overview of thermoelectricity applied to semiconductors materials [6].

Thermoelectricity is about electric current flow driven by a temperature difference. If we consider a semiconductor, the expression for the current can be write as:

$$I = \frac{1}{q} \int_{-\infty}^{+\infty} dE G(E) (f_1(E) - f_2(E)) \quad (1.6)$$

where the difference in  $f_1$  and  $f_2$  has been driven by the difference in electrochemical potentials  $\mu_1$  and  $\mu_2$  and these can be driven by a temperature difference,  $f_1$  and  $f_2$  can be written as:

$$f_1(E) = \frac{1}{\exp\left(\frac{E-\mu_1}{kT_1}\right) + 1}, f_2(E) = \frac{1}{\exp\left(\frac{E-\mu_2}{kT_2}\right) + 1} \quad (1.7)$$

figure 1.3 shows two contacts with the same electrochemical potential ( $\mu$ ) at different

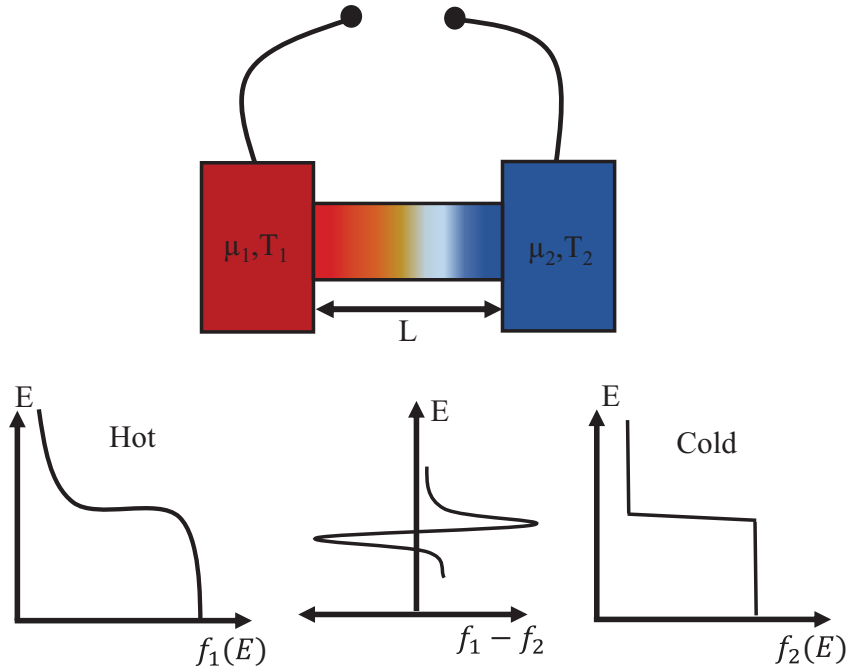


Figure 1.3: Illustration of Two contacts with the same electrochemical potential  $\mu$  at different temperatures.

temperatures. Near -equilibrium and small temperature difference, one can show that:

$$(f_1 - f_2) \approx - \left( - \frac{\partial f_0}{\partial E} \right) \frac{E - E_F}{T} \Delta T \approx \frac{\partial f}{\partial E} (\mu_1 - \mu_2) + \frac{\partial f}{\partial T} (T_1 - T_2) \quad (1.8)$$

We could write approximately the current flow as:

$$I = G(V_1 - V_2) + G_S(T_1 - T_2) \quad (1.9)$$

where we have defined  $V_1, V_2$  as  $\mu_1/q$  and  $\mu_2/q$  respectively and then, the conductance is given by:

$$G = \int_{-\infty}^{+\infty} dE G(E) \left( \frac{\partial f_0}{\partial \mu} \right) = \int_{-\infty}^{+\infty} dE G(E) \left( -\frac{\partial f_0}{\partial E} \right) \quad (1.10)$$

and the new coefficient:

$$G_S = \frac{1}{q} \int_{-\infty}^{+\infty} dE G(E) \left( \frac{\partial f_0}{\partial T} \right) = \int_{-\infty}^{+\infty} dE G(E) \left( -\frac{\partial f_0}{\partial E} \right) \frac{E - \mu_0}{qT} \quad (1.11)$$

Energy states with energy  $E$  greater and lesser than  $\mu_0$ , contribute with opposite signs to the thermoelectric coefficient  $G_S$ . In order to find a material with high Seebeck coefficient,  $S$  one would try to choose a material with all its density of states on one side of  $\mu_0$  since anything on the other side contributes with an opposite sign and brings it down. If we consider now a short circuit, the current is given by:

$$I_{SC} = G_S(T_1 - T_2) \quad (1.12)$$

Experimentally what is often measured is the open circuit voltage:

$$V_{0C} = -\frac{I_{SC}}{G} = -\frac{G_S}{G}(T_1 - T_2) \quad (1.13)$$

For  $n$ -type semiconductor, for example,  $G_S$  is positive, so that Eq.(1.7) tells us that  $V_{0C}$  is negative if  $T_1 > T_2$ . This means that the contact with the higher temperature has a negative electron voltage and hence a positive conventional voltage. By convention this is defined as a negative Seebeck coefficient.

$$S \equiv \frac{V_{0C}}{T_1 - T_2} = -\frac{G_S}{G} \quad (1.14)$$

## 1.4 The Figure of Merit

In order to compare different materials and their thermoelectric properties, one needs to take into account the thermal and electrical conductivities, that is to say, for a high efficiency thermoelectric material, a high electrical conductivity, a low thermal conductivity and a large Seebeck coefficient are needed. The relationship between these parameters and the material's efficiency is known as the figure of merit  $ZT$  and the best candidates for a large  $ZT$  are semiconductor materials.

$$ZT = \left( \frac{S^2 \sigma}{\kappa} \right) T \quad (1.15)$$

where  $S$  is the Seebeck coefficient,  $\sigma$  is the electrical conductivity,  $\kappa$  is the total thermal conductivity and  $T$  is the temperature. The thermal conductivity can be separated into two terms, one from free charge ( $\kappa_e$ ) and the other from lattice vibrations ( $\kappa_L$ ) contributions

as:  $\kappa = \kappa_e + \kappa_L$ . In semiconductors lattice vibrations - phonons - dominate the thermal conductivity with contribution from charge transport below 10%. Here two approaches were used to calculate the charge thermal conductivity contribution: (a) VASP and BoltzTraP packages for SnSe study and (b) the Wiedeman-Franz law for ITO and  $\text{Sb}_2\text{Se}_3$  calculations. The phonon thermal conductivity was calculated using a modified Debye-Callaway model described below. In the last years research has focused on many different aspects of electronic band structure engineering and thermal conductivity minimization strategies, including finding new materials with larger  $S$  values [7-9].

The increase of  $ZT$  values for bulk materials has been limited by the fact that  $S$ ,  $\kappa$ , and  $\sigma$ , are interdependent. On one hand, an increasing density of free charge carriers that can increase  $\sigma$ , reduces  $S$  and increases  $\kappa$ . On the other hand, the increase of  $\sigma$  without decreasing  $S$  requires reducing the density of crystal defects, which will increase  $\kappa$  as well. An idea to bypass this interdependence consists in growing low-dimensional structures such as quantum dots and nanowires, where phonons-boundaries scattering reduces  $\kappa$  without changing the properties of the material at the scale of the electrons scattering events; at the same time the asymmetric density of states near the Fermi level in nanostructures can increase  $S$  [2,4,10,11]. Following this idea, a  $ZT = 2$  at 300K was reported in 2002 for a quantum-dots superlattice [3]. In 2012 a  $ZT$  value of  $\sim 2.2$  at 915K was reported in a heterostructure where phonon scattering at various scale lengths was promoted by introducing hierarchical architecture design in nanostructured a PbTe-based system [12,13]. The reason for the high  $ZT$  is the structure of the system boundaries

at the atomic, nano-, and meso- scales that is capable of producing efficient scattering events for phonons over a broad range of wavelengths.

## 1.5 Wiedeman - Franz Law

The total thermal conductivity  $\kappa$  can be separated in two terms, one is the contribution from charges and the other from lattice vibrations, by phonons:  $\kappa = \kappa_e + \kappa_{ph}$  where  $\kappa_e$  is the electron thermal conductivity and  $\kappa_{ph}$  is the lattice thermal conductivity. The electron's contribution to the thermal conductivity can be related to the electrical conductivity through the Wiedeman - Franz law approximation [14], assuming no current flow as:

$$\kappa_e = \frac{1}{3} C_e v_F^2 \tau_E \quad (1.16)$$

where  $\tau_E$  is the energy relaxation time of electrons and is an average of  $\tau$ , and  $C_e$  is the volumetric specific heat of electrons.  $\tau_E$  represents the average time for an electron to lose its excess energy. In general, the energy relaxation time can be different from the momentum relaxation time however, the two relaxation times are very close. Neglecting the difference between the relaxation times, one gets:

$$L = \frac{\kappa_e}{\sigma T} = \frac{m C_e v_F^2}{3 n T e^2} = \frac{\pi^2}{3} \left( \frac{k_B}{e} \right)^2 = 2.44 \times 10^{-8} [\text{W}\Omega\text{K}^{-2}] \quad (1.17)$$



Using ( $\kappa_e = \sigma LT$ ), where  $\sigma$  is the experimental electrical conductivity,  $T$  the absolute temperature and the constant  $L$  is the Lorentz number, the electron's contribution to the thermal conductivity for the here studied  $\text{Sb}_2\text{Te}_3$  nanobelts were calculated in the degenerarte limit. Hyun-Sik et. al. [15] proposed the equation:

$$L = 1.5 + \exp\left(-\frac{|S|}{116}\right) \quad (1.18)$$

where  $L$  is in  $10^{-8} \text{ W}\Omega \text{ K}^{-2}$  and  $S$  is in  $\mu\text{V/K}$ . This relation is a first order correction independent of the temperature and doping. Here, this relation was used to calculate the charge electrical conductivity of ITO nanowires and  $\text{Sb}_2\text{Se}_3$  hexagonal nanotubes.

## 1.6 Modified Debye-Callaway Model

The thermal conductivity due to electrons is small compared with the phonon's contribution, the largest contribution to the total thermal conductivity comes from lattice vibrations, by phonons. The next is an expression for a modified Debye-Callaway model [16], which gives s good approximation of the phonon's thermal conductivity  $\kappa_{ph}$ :

$$\kappa_{ph}(T) = \frac{k_B}{2\pi^2 v_s} \left(\frac{k_B T}{\hbar}\right)^3 \int_0^{T_D/T} \frac{x^4 e^x}{\tau_{ph}^{-1} (e^x - 1)^2} dx \quad (1.19)$$

with:

$$\tau_{ph}^{-1} = \tau_I^{-1} + \tau_D^{-1} + \tau_U^{-1} + \tau_B^{-1} + \dots \quad (1.20)$$

$$= A\alpha^4 T^4 x^4 + RTx + B\alpha^2 T^3 x^3 \exp\left(-\frac{T_D}{T}\right) + \frac{v_s}{t} + \dots \quad (1.21)$$

Where  $x = \frac{\hbar\omega}{k_B T}$  is the reduced phonon frequency,  $\hbar$  is the Planck constant,  $k_B$  is the Boltzmann constant,  $v_s$  is the speed of sound in the material,  $T_D$  is the Debye temperature and  $T$  is the absolute temperature. The fitting parameters are  $A$  for point defects,  $R$  for dislocations,  $B$  for umklapp events and  $t$  is related to the boundary conditions, in this case it is related to the diameter or thickness of the nanowire or nanotube.  $R$  and  $B$  were considered as constants and  $t$  and  $A$  were used as fitting parameters to described the measured data. This model was used to understand the nature of the thermal phonon's conductivity in ITO and SnSe nanowires and Sb<sub>2</sub>Se<sub>3</sub> nanotubes.

## 1.7 VASP and BoltzTraP Packages - General Aspects

### 1.7.1 VASP

In order to understand the observed transport response in SnSe nanowires, density functional theory (DFT) calculations were performed using the Vienna Ab Initio Simulation

Package (VASP) [17]. The many-body GW approximation was implemented with the projector augmented wave (PAW) scheme [18] and the generalized gradient approximation of Perdew, Burke and Ernzerhof (GGA-PBE) [19] for the electronic correlation functional. The energy cut-off for the plane wave expansion was 450 eV.

The Brillouin zones of the bulk SnSe were sampled in a gamma centered grid with a k-point mesh of  $5 \times 15 \times 15$ . To obtain an accurate DOS, the k-point mesh of the non-self-consistent was increased to  $11 \times 33 \times 33$ . Atomic positions and unit cell vectors were relaxed until all the forces and components of the stress tensor were below  $0.001 \text{ eV}\text{\AA}^{-1}$ . For the calculations bulk parameters were used because the diameter of the studied nanowires were greater than 100 nm and calculations show a bulk behavior in nanowires with diameters greater than 10 nm.

### 1.7.2 BoltzTraP

The transport properties for SnSe were calculated based on the Boltzmann transport equation under the rigid band and constant relaxation time approximations as implemented on the BoltzTraP package [20]. For the calculation of the semi-classic transport coefficients, the code used a mesh of band energies and was interfaced to the WIEN2K, ABINIT, SIESTA, VASP and QuantumExpresso. This package has been used to study several thermoelectric materials with good results, and can calculate  $S$  as a function

---

of the chemical potential at different temperatures. By interpolating the experimental data with the electron transport calculations the Fermi energy, charge density, electron mobility and electron thermal conductivity as function of temperature was obtained.

## 1.8 References

- [1] Bell, L.E., Cooling, heating, generating power, and recovering waste heat with thermoelectric systems. *Science*, **2008**. 321(5895): p. 1457-1461.
- [2] Hicks, L. and M. Dresselhaus, Effect of quantum-well structures on the thermoelectric figure of merit. *Physical Review B*, **1993**. 47(19): p. 12727.
- [3] Harman, T., et al., Quantum dot superlattice thermoelectric materials and devices. *Science*, **2002**. **297**(5590): p. 2229-2232.
- [4] Dresselhaus, M.S., et al., New Directions for Low-Dimensional Thermoelectric Materials. *Advanced Materials*, **2007**. 19(8): p. 1043-1053.
- [5] DiSalvo, F.J., Thermoelectric Cooling and Power Generation. *Science*, **1999** 285(5428): p. 703-706.
- [6] Datta, S., Lessons from nanoelectronics: a new perspective on transport. Vol. 1. **2012**: World Scientific publishing company.
- [7] Snyder, G.J. and T.S. Ursell, Thermoelectric efficiency and compatibility. *Physical review letters*, **2003**. 91(14): p. 148301.
- [8] Heremans, J.P., Thermoelectric materials: The anharmonicity blacksmith. *Nature Physics*, **2015**.

- 
- [9] He, J. and T.M. Tritt, Advances in thermoelectric materials research: Looking back and moving forward. *Science*, **2017**. 357(6358): p. 9997.
- [10] Nielsch, K., et al., Thermoelectric Nanostructures: From Physical Model Systems towards Nanograined Composites. *Advanced Energy Materials*, **2011**. 1(5): p. 713-731.
- [11] Heremans, J.P., et al., When thermoelectrics reached the nanoscale. *Nature nanotechnology*, **2013**. 8(7): p. 471-473.
- [12] Biswas, K., et al., High-performance bulk thermoelectrics with all-scale hierarchical architectures. *Nature*, **2012**. 489(7416): p. 414-418.
- [13] Zhao, L.-D., V.P. Dravid, and M.G. Kanatzidis, The panoscopic approach to high performance thermoelectrics. *Energy & Environmental Science*, **2014**. 7(1): p. 251-268.
- [14] Chen, G., Nanoscale energy transport and conversion. **2005**.
- [15] Kim, H.-S., et al., Characterization of Lorenz number with Seebeck coefficient measurement. *APL materials*, **2015**. 3(4): p. 041506.
- [16] Callaway, J., Model for lattice thermal conductivity at low temperatures. *Physical Review*, **1959**. 113(4): p. 1046.
- [17] Kresse, G. and J. Furthmüller, Efficiency of ab-initio total energy calculations for metals and semiconductors using a plane-wave basis set. *Computational Materials*

- 
- Science, **1996**. 6(1): p. 15-50.
- [18] Blochl, P.E., Projector augmented-wave method. Physical Review B, **1994**. 50(24): p. 17953.
- [19] Perdew, J.P., K. Burke, and M. Ernzerhof, Generalized gradient approximation made simple. Physical review letters, **1996**. 77(18): p. 3865.
- [20] Madsen, G.K. and D.J. Singh, BoltzTraP. A code for calculating band-structure dependent quantities. Computer Physics Communications, **2006**. 175(1): p. 67-71.

# Chapter 2

## Synthesis, Characterization Techniques and Experimental Setup

---

### 2.1 Synthesis of Nanowires: Chemical Vapor Deposition (CVD) via Vapor Liquid Solid (VLS)

Chemical vapor deposition (CVD) is a chemical process used to produce high quality and performance solid materials [1]. CVD is often used in the semiconductor industry to produce a lot different types and shape of materials, thin films, nanowires, nanoflakes, nanotubes, 2-D materials and many others. In typical CVD, the wafer substrate is exposed to one or more gas-phase precursors, which react and/or decompose on the substrate surface to produce the desired deposit. Frequently, volatile by-products are also produced, which are removed by gas flow through the reaction chamber. Nanofabrication processes widely use CVD to deposit materials in various forms, including: monocrystalline, polycrystalline, amorphous and epitaxial. Figure 2.1 show a schematic setup representation of typical CVD.



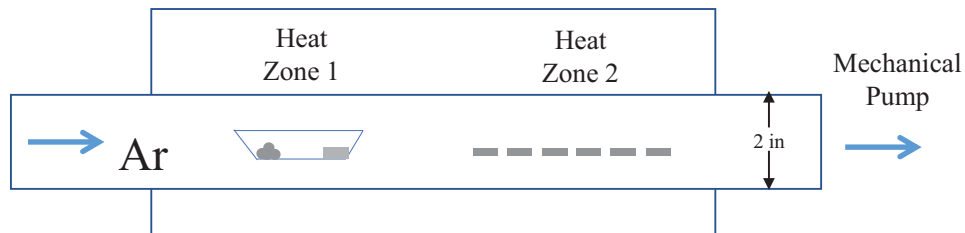


Figure 2.1: CVD Schematic Setup Representation

The Vapor Liquid Solid (VLS) is a mechanism for the growth of one dimensional structures, for example nanowires and nanotubes, from CVD process. VLS introduces a catalytic liquid alloy phase which absorb a vapor to supersaturation levels, and from which the crystal growth can occur from nucleated seed at the liquid-solid interface [2]. Figure 2.2 shows a schematic representation of VLS mechanism for the ITO nanowires case.

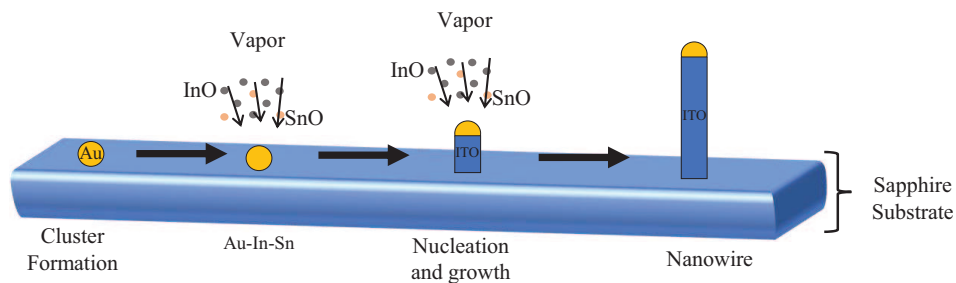


Figure 2.2: Schematic representation of VLS mechanism for growth ITO nanowires.

Using VLS process, SnSe and ITO nanowires were successfully synthesized with different diameters and lengths, using Au as catalyst.

## 2.2 Experimental Characterization Techniques

### 2.2.1 X-ray Diffraction (XRD)

XRD is a practical tool for the routine identification of the crystallographic structure of materials. In standard XRD systems, X-rays are generated when high-energy electrons are made to collide with a metal target within a sealed tube under high vacuum. The source of electrons normally come from a tungsten filament which connects to a high voltage. The wavelength of the X-ray is characteristic of the metal target, copper is must used target material with  $\lambda = 1.64 \text{ \AA}$ . In their pioneering work, Laue and Bragg (1912) found that when a monochromatic x-ray beam interacts with the sample it disperses in all directions but, when the interaction is with the crystallographic planes in a specific angles, the interference is constructive. The relationship between the diffraction angle  $\theta$ , the inter planar spacing  $d_{hkl}$ , the wave length of the X-ray  $\lambda$  and the order of diffraction  $n$  is given by the Bragg's law:

$$n\lambda = 2d_{hkl}\sin\theta \quad (2.1)$$

The X-ray diffraction pattern is known as the fingerprint of that particular material because it produces specific crystalline diffraction lines at specific diffraction angles, by which it may be identified. A collection of diffraction patterns for various classes of materials allow the identification of an unknown phase pattern when it matches the pattern of a known phase. An XRD pattern is characterized by a set of diffraction

intensities, as well as the peak in the pattern of maximum intensity [3].

In the case of nanowires on a substrate, the pattern is from a large area  $\sim \mu m^2$ , over which nanowires and also micro-crystals grow with different features and sizes, then the pattern involves all these structures, including nanowires. As a consequence of this, the results were compared with selective area electron diffraction (SAED-TEM) results from a single measured nanowire on the micro-device. The results showed that SnSe nanowires and  $Sb_2Se_3$  had an orthorhombic crystal structure and ITO nanowires had a cubic crystal structure figure 2.3 shows a crystal parameters illustration.

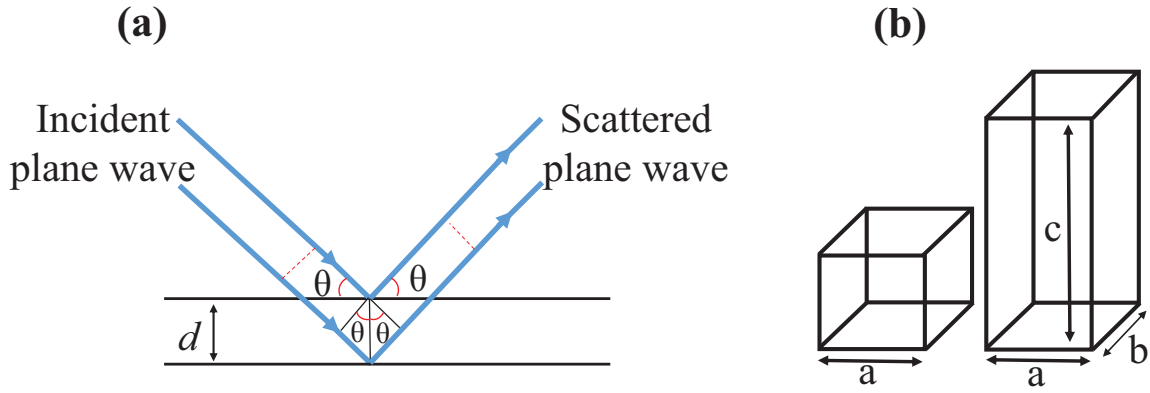


Figure 2.3: Illustration of (a) incident and scattered plane wave into a interplanar  $d$  (b) Crystal parameters for Cubic, Orthorhombic and Hexagonal lattice

In the case of an orthorhombic lattice, the relationship between the interplanar distance and the lattice parameters is:

$$\frac{1}{d_{hkl}^2} = \frac{h^2}{a^2} + \frac{k^2}{b^2} + \frac{l^2}{c^2} \quad (2.2)$$

and, in the case of a cubic lattice:

$$\frac{1}{d_{hkl}^2} = \frac{(h^2 + k^2 + l^2)}{a^2} \quad (2.3)$$

In this work the above relationships were used to found the parameters  $a$ ,  $b$  and  $c$  and to obtain the exact match with the data from SAED-TEM. The XRD measurements was carried out bu using a Siemens D5000 diffractometer. This equipment operate on the basis of Bragg-Brentano geometry,  $\text{CuK}_\alpha$  radiation and an energy-dispersive solid state detector.

### 2.2.2 Scanning Electron Microscopy (SEM)

SEM is a most versatile tool for the characterization of nano-materials. It create images and analyses of the sample by scanning a focused electron beam. The electrons interact with atoms in the sample, generating different signals that contain information about the samples surface, topography and composition (see a related illustration in figure [2.4](#)). SEM can achieve resolutions better than 1 nm, with magnifications up 1 million times. Specimens can be observed in high vacuum, in low vacuum, in wet conditions (in environmental SEM) and at a wide range of cryogenic or elevated temperatures [5]. In this work, Jeol JSM-7500F and Hitachi S-5500 SEMS were used. The SEM is an important tool in the study of synthesis parameters and the preparation of the samples for thermoelectric measurements.

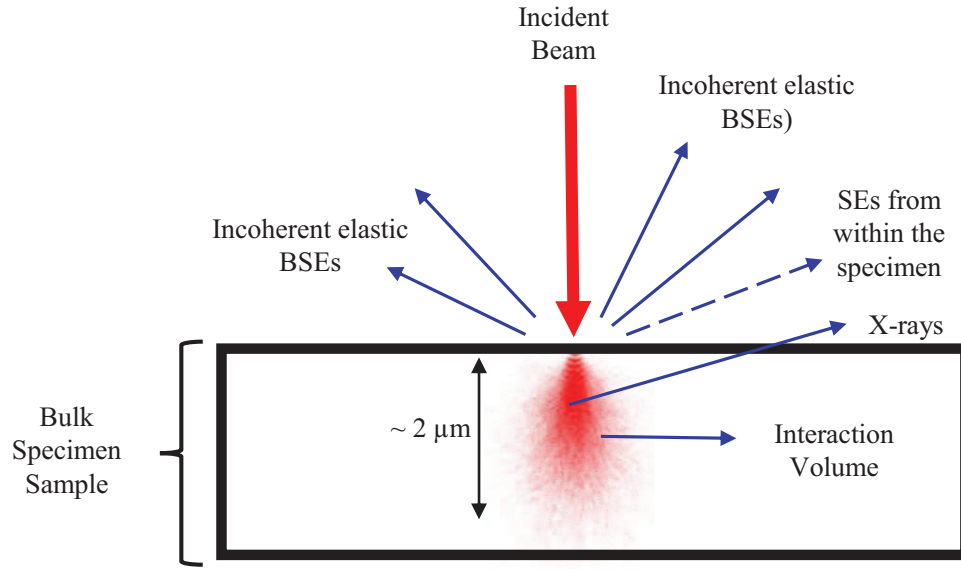


Figure 2.4: Illustration of different signals from a typical electron beam interaction with a bulk sample in a SEM.

### 2.2.3 Transmission Electron Microscopy (TEM)

TEM is a very powerful tool for material science. In a TEM a high energy beam of collimated electrons is transmitted through a very thin sample, less than 100 nm thick. As a product of the interactions between the electrons and the sample, crystal structure features and diffraction patterns can be obtained; dislocations and grain boundaries can be resolved, and chemical analyses can be made. The sample's image under transmission is magnified and focused onto an imaging device with resolution within the atomic scale.

Transmission electron microscopes are capable of imaging at a significantly higher resolution than light microscopes, owing to the smaller de Broglie wavelength of electrons. This enables the instrument to capture images as small as a single column of atoms,

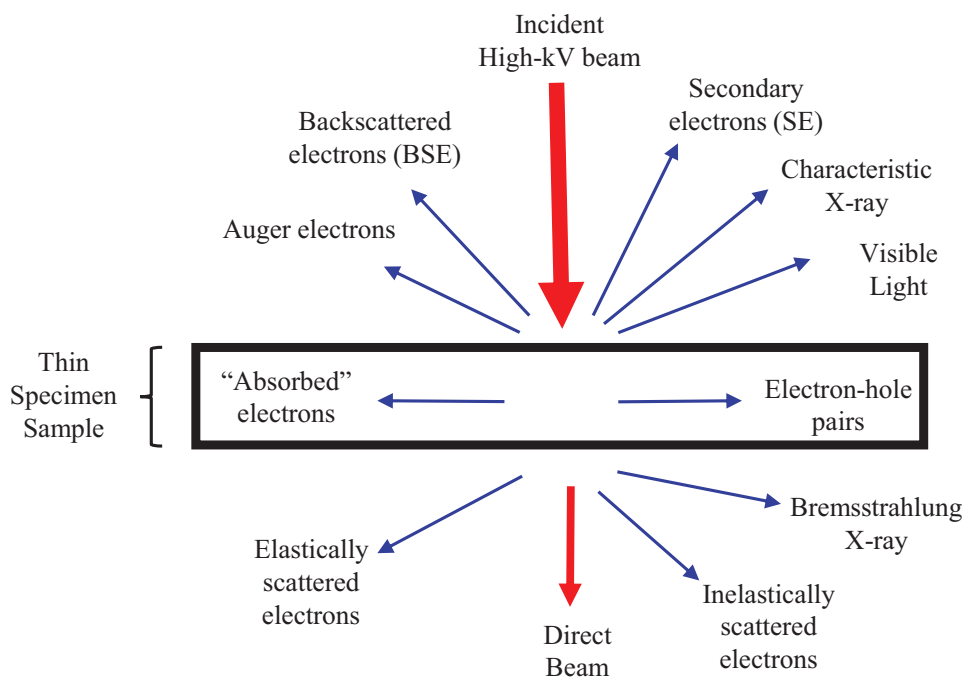


Figure 2.5: Signals generated when a high-energy beam of electrons interacts with a thin specimen. Most of these signals can be detected in different types of TEM.

which is thousands of times smaller than a resolvable object seen in a light microscope. Transmission electron microscopy is a major analytical method in the physical, chemical and biological sciences.

When the charge of the incident high voltage electron beam interacts with the positively charged core of the atoms it creates an outgoing electron and generates a wide range of secondary signals from the specimen, some of which are showed in the Figure 2.5. Conventional TEM uses only elastic signals for diffraction and spatial imaging. TEM can be equipped with analytical tools, like spectrometers: (a) energy dispersive X-ray spectrometry (EDS) where the characteristic X-ray from the chemical elements are used to determine elemental composition and relative concentration (b) electron energy-loss

spectrometry (EELS) where the information on local chemistry and structure is obtained from the analysis of the energy losses of the electron. A Scanning Transmission Electron Microscope (STEM) is used for high resolution TEM (HR-TEM) to form images of columns of atoms through the so-called phase-contrast imaging. In this technique, the phase of the diffracted electron wave is preserved and interferes constructively or destructively with the phase of the transmitted wave [5].

In this study a JEOL JEM-ARM200F TEM was used, incorporating a spherical aberration corrector for the electron optics system getting scanning transmission image (STEM-HAADF) resolutions of 0.08 nm.

#### 2.2.4 Focused Ion Beam (FIB)

The JEOL JEM9310 FIB used in this work operates similar to a SEM, using a focused beam to create an image. In this case the beam is a  $\text{Ga}^+$  ion beam but, similar to SEM, the image is generated by the intensity of secondary electrons generated when the Ga ion beam scans the sample. The magnification is  $\sim 100,000$  times [5].

Different to an electron beam, the ion beam in the FIB erodes the sample. When a  $\text{Ga}^+$  ion is focused on the target sample, it creates a cascade of events which results in the ejection of sputtered particles, in this way a FIB is used to do very small and precise cuttings, and the most common application is to prepare specimen samples for TEM analysis.

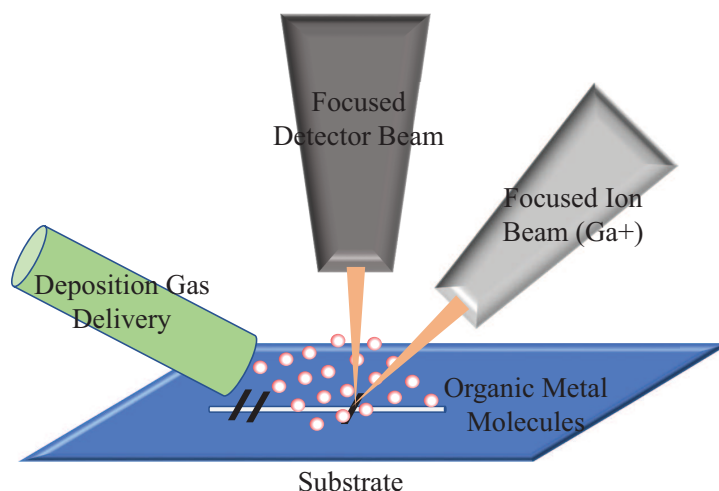


Figure 2.6: Focused Ion Beam diagram representation - the organometallic is used to deposit contacts

Another feature that is used in the FIB is the ion beam-assisted chemical vapor deposition. The deposition of metals is used extensively in silicon semiconductor device modification, to protect the top surface of interest. A needle is brought to within 100-200 mm of the target surface, then a Pt organometallic is injected from the needle near where the  $\text{Ga}^+$  beam scans over the specimen region. The ion beam decomposes the gas and promotes by charging the deposition of Pt over the area irradiated by the beam, while the byproduct is removed through the vacuum system.

In this way, Pt contact depositions were performed into a the JEOL JEM FIB 9310, operated at 30 kV. This FIB has a resolution of 10 nm, provides a maximum current of  $10\ \mu\text{A}$  and is equipped with two grounded stages with three-axis translation, rotation and tilt capabilities. 10 different beam diameters can be used, but for deposition a beam number 9 was used in order to decrease the beam damage in the nanowire and device



surface.

## 2.3 Experimental Thermoelectric Device and Setup

### 2.3.1 Thermoelectric Device

The suspended specialized micro resistance thermometry device were supplied by Dr. Michael T. Pettes and Dr. Li Shi from the University of Texas at Austin and were used to measure  $S$ ,  $\sigma$  and  $\kappa$  in a single nanowire and single hexagonal nanotubes [6,7]. Figure 2.7 shows a different magnification images of a micro-device connected to chip carrier using Al wire.

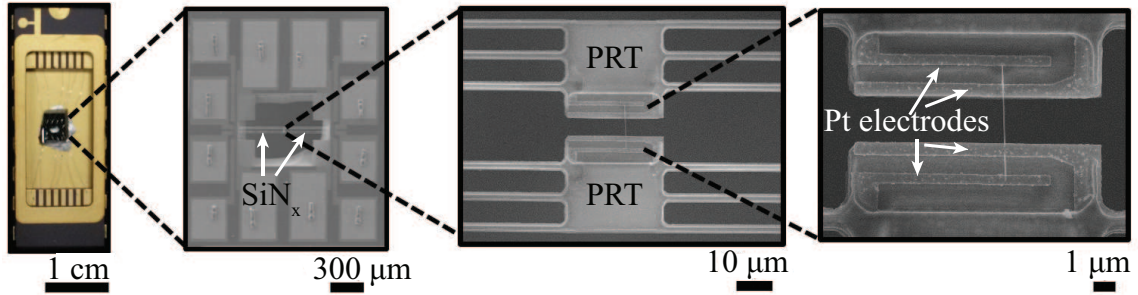


Figure 2.7: Different magnification of micro-device into a chip carrier for a SnSe measured sample

The suspended micro-device consists of two adjacent  $20\mu\text{m} \times 20\mu\text{m}$  low-stress silicon nitride ( $\text{SiN}_x$ ) membranes each suspended with six  $420\mu\text{m}$ -long and  $2\mu\text{m}$ -wide  $\text{SiN}_x$  beams, four to connect a one platinum serpentine resistance thermometer (PRT) and two for  $1\mu\text{m}$ -wide Pt electrodes patterned on each membrane. PRT and electrodes were

created using electron beam lithography (EBL) and reactive ion etching (RIE) procedures to create the electrical leads and contact pads into the platinum film, followed by the deposition of a dielectric layer film onto the top to prevent any shorting of the measuring device.

The bottom side of the wafer was then patterned with contact photolithography and RIE process, to expose silicon that would be removed to create the through hole in each device, allowing the study of crystal structure and chemical composition of the sample on the suspended device by using TEM or STEM, selective area electron diffraction (SAED) and the energy dispersive X-ray spectroscopy (EDS). In this way, the thermoelectric measurements can be done in a four probe configuration (two sample-to-electrodes contacts in each membrane) that allows to eliminate the thermal and electrical contact resistances in the measurements.

### 2.3.2 Experimental Setup

For the nanowires and nanotubes measurements, each micro-device with the integrated sample was positioned into a Janis ST-100 cryostat connected to a Pfeiffer Balzers TCP121 turbo pumping system to create a  $\sim 5 \times 10^{-6}$  torr vacuum. The environment temperature surrounding the microdevice was controlled using a Lakeshore 330 temperature controller and a liquid nitrogen cold finger for all sub-room temperature measurements. The microdevice was connected to two Stanford Research Systems SR830 DSP

lock-in amplifiers which measured the first harmonic component of the AC voltage drop across the heating and sensing membranes using an AC current of  $0.5 \mu\text{A}$ , at frequencies of 1.0 kHz for the heating membrane and 200.0 Hz for the sensing membrane.

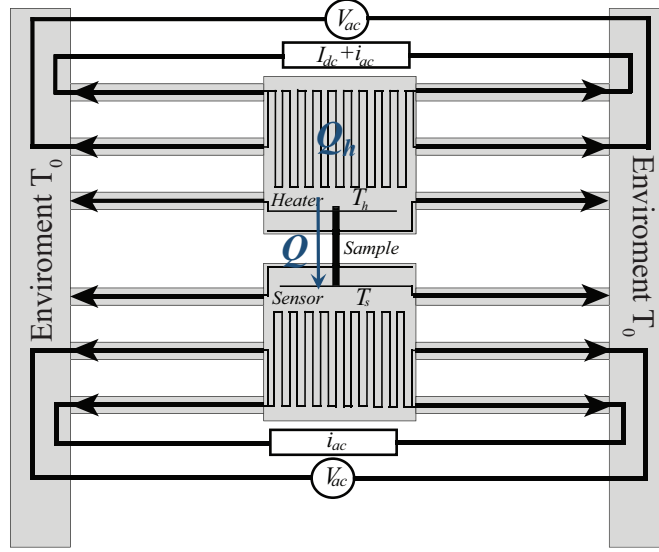


Figure 2.8: Experimental thermal resistance diagram and schematic setup for thermal resistance or conductance measurements of individual Nanowire

A National Instruments BNC-2090 DAQ board was used as an interface with the experiment and sourced a DC voltage which was used to raise the temperature of the heating membrane with a current between zero and  $\sim 10 \mu\text{A}$ . A Stanford Research Systems SR570 low-noise current amplifier was used to measure the DC component of the coupled  $AC + DC$  current being supplied to the heating membrane and two Stanford Research Systems SR560 were used to measure the thermoelectric voltage generated by the sample. LabVIEW software was used to control and collect the various voltages and current readings as a function of the provided DC voltage. A schematic diagram of the experimental setup is shown in figure 2.8. When a direct current ( $I$ ) was supplied to

one PRT to raise the temperature of one membrane, part of the Joule heat generated in the heating membrane,  $Q$  was conducted through the sample to the other (sensing) membrane.

### 2.3.3 Thermoelectric and thermal conductance measurements

The  $I_{dc}$  current supplied to the platinum resistance thermometer (PRT) on the heating membrane heats up this side and part of the Joule heat generated is conducted through the sample to the sensing membrane. Figure 2.9(c,d) shows a 3 completing cycles from the heating and sensing membranes.

$$\Delta T_h(I_{dc}) \equiv T_h(I_{dc}) - T_0 \quad (2.4)$$

$$\Delta T_s(I_{dc}) \equiv T_s(I_{dc}) - T_0 \quad (2.5)$$

where  $T_0$  is the substrate temperature. A change in temperature induces a change in electrical resistance of each PRT which is translated into temperature by measuring the temperature coefficient of resistance  $\alpha \equiv \left( \frac{dR/dT}{R(T_0)} \right)$  of each PRT at each  $T_0$ .

The thermal resistance of the 6 beams supporting each membrane can then be obtained as:

$$R_B = \frac{\Delta T_H + \Delta T_s}{Q_h + Q_L} \quad (2.6)$$

where  $Q_h$  is the Joule heat dissipation in the PRT on the heating membrane and  $Q_L$

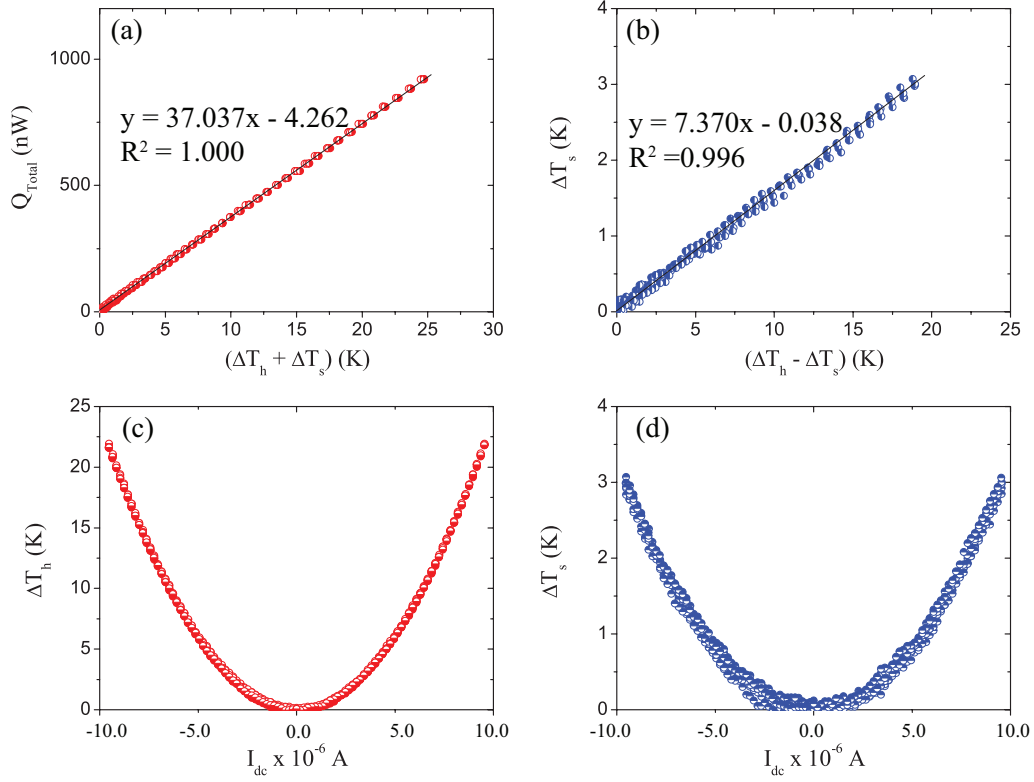


Figure 2.9: (a) Measured total heat  $Q_{Total} = Q_h + Q_L$  plotted as function of  $T_h + T_s$  for sample 2 of  $\text{Sb}_2\text{Te}_3$  nanobelt, the slope give us the total thermal conductance  $G_B$ . (b) The obtained  $\Delta T_s$  as a function of  $\Delta T_h - \Delta T_s$ , the slope yields  $G_m/G_B$ . (c) and (d) are the change in temperature of the heating membrane  $\Delta T_h$  and sensing membrane  $\Delta T_s$  as a function of ramped  $I_{dc}$  for 3 cycles

is the Joule heat dissipation in the two identical Pt leads supplying the current to the heating PRT. Then, the total measured thermal resistance of the sample (see figure 2.9) is obtained as:

$$R_{total} \equiv R_{C,1} + R_S + R_{C,2} = \frac{\Delta T_h - \Delta T_s}{Q} \quad (2.7)$$

where  $R_S$  is the thermal resistance of the suspended segment of the sample,  $R_{C,1}$  and

$R_{C,2}$  are the contact thermal resistances between the sample and the two membranes and  $Q$  are the heat conducted through the six beams of the sensing membrane to the substrate.

Using the four Pt contacts deposited on the sample, two thermoelectric voltages generated by the sample due to the temperature difference are generated:

$$S_{14} = \frac{V_{14}}{T_h - T_s} \quad (2.8)$$

$$S_{23} = \frac{V_{23}}{T_h - T_s} \quad (2.9)$$

The total contacts thermal resistance can be obtained from the ratio ( $\gamma$ ) between  $S_{14}$  and  $S_{23}$ :

$$\gamma \equiv \frac{S_{14}}{S_{23}} = \frac{T_1 - T_4}{T_2 - T_3} \quad (2.10)$$

Figure 2.10 shows the heat transfer between the two membranes through the suspended sample. The thermal contact resistance can be calculated using the fin model resistance relationship:

$$R_{C,i} = \frac{1}{\kappa A m \tanh(m L_{C,i})}, i = 1 \text{ or } 2 \quad (2.11)$$

where  $\kappa$  is the thermal conductivity and  $A$  is the cross section area of the sample,  $L_{C,i}$  is the length of sample segment in the contact with the membrane and  $m$  is defined as:

$$m = \sqrt{\frac{hw}{\kappa A}} \quad (2.12)$$

where  $h$  is the thermal contact conductance per unit area and  $w$  is the diameter of the sample. With the use of a sensitive AC measurement of the differential electrical resistances of the two PRTs, the measurement method can achieve a sensitivity on the order of  $1 \times 10^{-10} \text{ WK}^{-1}$  in the measured thermal conductance,  $G_m \equiv \frac{1}{R_m}$ . To obtain the sample thermal conductance:

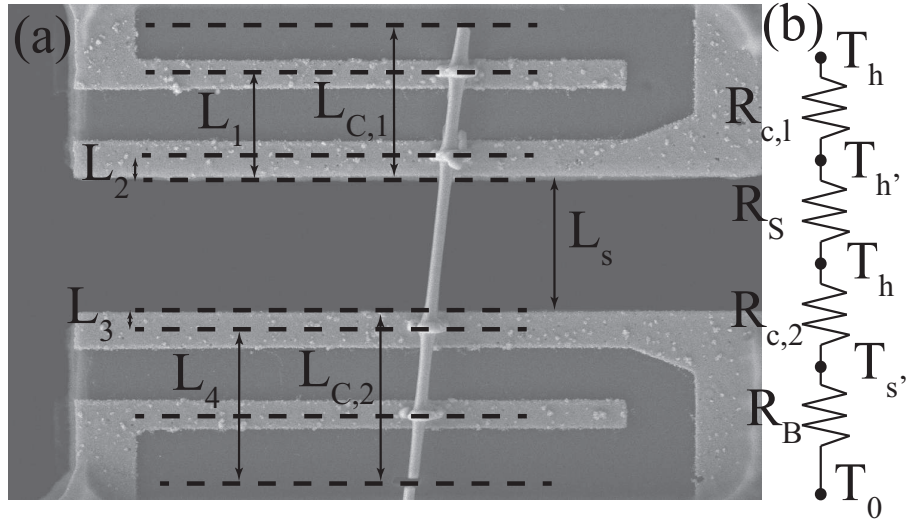


Figure 2.10: Schematic diagram of the nanowire suspended between two suspended membranes indicating various length segments for the fin model analysis.

The thermal resistance of the suspended segment of the sample:

$$R_S = \frac{L_S}{\kappa A} \quad (2.13)$$

where  $L_S$  is the length of the suspended segment. From figure 2.10 we have:

$$Q = \frac{T_h - T_h'}{R_{C,1}} = \frac{T_h' - T_{s'}}{R_S} = \frac{T_{s'} - T_s}{R_{C,2}} \quad (2.14)$$

According with the fin model temperature profile:

$$\frac{T_h - T_i}{T_h - T'_h} = \frac{\cosh(m(L_{C,1} - L_i))}{\cosh(mL_{C,1})}, i = 1 \text{ or } 2 \quad (2.15)$$

and

$$\frac{T_i - T_s}{T'_s - T_s} = \frac{\cosh(m(L_{C,2} - L_i))}{\cosh(mL_{C,2})}, i = 3 \text{ or } 4 \quad (2.16)$$

from equations 2.13 and 2.15, 2.16 we obtain:

$$\gamma_{14} \equiv \frac{T_1 - T_4}{T'_h - T'_s} = 1 + \frac{1 - \cosh(m(L_{C,1} - L_1)) / \cosh(mL_{C,1})}{L_s m \tanh(mL_{C,1})} + \frac{1 - \cosh(m(L_{C,2} - L_4)) / \cosh(mL_{C,2})}{L_s m \tanh(mL_{C,2})} \quad (2.17)$$

$$\gamma_{23} \equiv \frac{T_2 - T_3}{T'_h - T'_s} = 1 + \frac{1 - \cosh(m(L_{C,1} - L_2)) / \cosh(mL_{C,1})}{L_s m \tanh(mL_{C,1})} + \frac{1 - \cosh(m(L_{C,2} - L_3)) / \cosh(mL_{C,2})}{L_s m \tanh(mL_{C,2})} \quad (2.18)$$

and

$$\gamma = \frac{T_1 - T_4}{T_2 - T_3} = \frac{\gamma_{14}}{\gamma_{23}} \quad (2.19)$$

And the following equation to calculate the ratio  $\alpha$  is obtained:

$$\alpha \equiv \frac{T_h - T_s}{T'_h - T'_s} = 1 + \frac{1}{L_s m} \left( \frac{1}{\tanh(mL_{C,1})} + \frac{1}{\tanh(mL_{C,2})} \right) \quad (2.20)$$

Using the  $\alpha$  and  $\gamma_{23}$  values calculated from the measured  $S_{14}$  and  $S_{23}$  at each temperature, the Seebeck coefficient, the sample thermal resistance, and the contact thermal resistance



are obtained as:

$$S = \alpha \frac{S_{23}}{\gamma_{23}} \quad (2.21)$$

$$R_S = R_{total}/\alpha \quad (2.22)$$

$$R_C \equiv R_{total} - R_S \quad (2.23)$$

## 2.4 References

- [1] Pierson, H.O., Handbook of chemical vapor deposition: principles, technology and applications. **1999** William Andrew.
- [2] Dhanaraj, G., et al., Springer handbook of crystal growth. **2010** Springer Science & Business Media.
- [3] Suryanarayana, C. and M.G. Norton, X-ray diffraction: a practical approach. **1998** New York, Plenum Publishing Corporation.
- [4] Chastain, J., R.C. King, and J. Moulder, Handbook of X-ray photoelectron spectroscopy: a reference book of standard spectra for identification and interpretation of XPS data. **1992** Physical Electronics Division, Perkin-Elmer Corporation Eden Prairie, Minnesota.
- [5] Williams, D.B. and C.B. Carter, The transmission electron microscope, in Transmission electron microscopy. **1996** Springer. p. 3-17.
- [6] Pettes, M.T., Experimental investigations of thermal transport in carbon nanotubes, graphene and nanoscale point contacts. **2011** The University of Texas at Austin.
- [7] Mavrokefalos, A., et al., Four-probe measurements of the in-plane thermoelectric properties of nanofilms. Review of scientific instruments, **2007** 78(3): p. 034901

# Chapter 3

## Thermoelectric Properties and Thermal Tolerance of Indium Tin Oxide Nanowires

---

### 3.1 Introduction

Transparent conducting oxides (TCO) combining high transparency and electrical conductivity are widely used in important technological applications. Indium tin oxide (ITO) is one of the most used TCO and plays an important role in diverse technologies [1] that include solar cells [2-5], light emitting diodes [6,7], gas sensors [8] and smart windows [9]. Due to the high crystallinity, large grains size, and high transparency in the visible spectral region ITO films are also used as transparent electrodes [8,9]. In the last years, reports show high performance synthesis of ITO nanowires, which makes these nanostructures promising electrode material due to their exceptional properties, such as large surface area, high crystallinity, low resistivity and reproducible synthesis via different techniques including carbothermal evaporation process [10], vapor transport method [11-15], pulsed laser ablation [6,16,17], thermal metal co-evaporation [18,19], electron beam

evaporation [20], co-precipitation-anneal method [21], electrospinning [22], DC sputtering [23], and electrochemically assisted deposition in template membranes [24].

The thermoelectric properties of ITO and its thermal tolerance expand the potential use of ITO nanowires, especially for applications in harsh and high temperature environments. As previously mentioned, thermoelectric nanomaterials are receiving great attention in recent years because they can interconvert thermal gradients and electric fields for power generation, waste heat recovery, or solid state refrigeration [25-29] with high efficiencies and nanostructured materials with moderate density of charge carriers show  $ZT$  higher than bulk values because the different size-dependent scaling trends for the electrical and thermal conductivities allow for the reduction of the long wavelength phonon mean free path by enhancing the surface scattering, thus reducing  $\kappa$  without affecting  $\sigma$  as strongly [30-34].

Many oxide semiconductors are chemically and thermally stable in air at high temperatures, what makes them good candidates for high temperature thermoelectric applications [26,35-37]. Thermoelectric studies on ITO thin films show a dependence of  $ZT$  on Sn concentration. The thermopower in ITO is negative indicating n-type behavior [38-41], Guilmeau et. al. [42] tuned the ITO-bulk transport properties through doping In sites with  $\text{Ti}^{4+}$ ,  $\text{Zr}^{4+}$ ,  $\text{Sn}^{4+}$ ,  $\text{Ta}^{5+}$ , and  $\text{Nb}^{5+}$ , finding a thermopower at room temperature of  $\sim 41 \mu\text{V/K}$  in case of  $\sim 1\%$  Sn; Zhu et. al. [43] found a maximum  $ZT$  of 0.15 at 1000 K using 5% Lu and 0.1% Sn concentrations. Other similar studies used Co [44], Zn

and Nd [45], Ge [46] and Ga [47] as dopants but none of these works have investigated size effects on the thermoelectric properties.

Here we report successful synthesis of high quality single-crystalline ITO nanowires with high temperature tolerance up to 1300°C. The correlation between the structural and thermoelectric properties of single nanowires with and without heat treatment and the corresponding changes in  $S$ ,  $\sigma$  and  $\kappa$  values is explained. The high temperature tolerance of ITO nanowires is then clarified for their potential use as building blocks in new thermoelectric devices that can operate in harsh environments.

## 3.2 Synthesis and Characterization

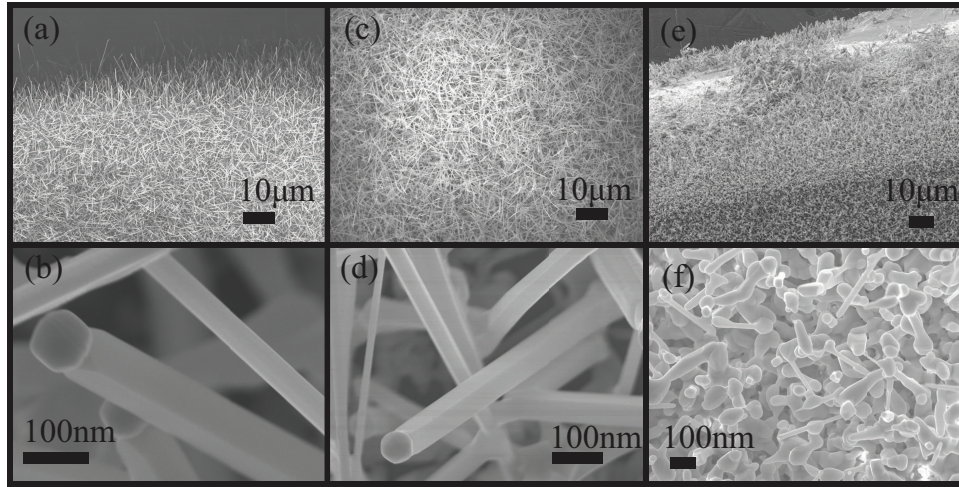


Figure 3.1: SEM images for ITO nanowires (a), (b) as-synthesized, (c), (d) After 1300°C annealing and (e), (f) After 1400°C annealing.

ITO nanowires were synthesized using a catalyst-assisted thermal VLS process, using

quartz and sapphire substrates coated with 1-3 nm Au films. As synthesized samples exhibited homogeneous and straight morphological features with lengths of up to several tens of micrometers as shown in Figures 3.1 (a, b). The samples were tested for high temperature tolerance by annealing them in air at different temperatures in 30 min intervals. According to SEM images, the overall morphology is preserved in the temperature range up to 1300°C as shown in figures 3.1 (c, d). Thermal treatment at higher temperatures resulted in evaporation and segregation of the material on the substrate. Figures 3.1e and 3.1f show the effect of 1400°C heat treatment. According to these results, three as prepared and three 1300°C annealed samples were studied.

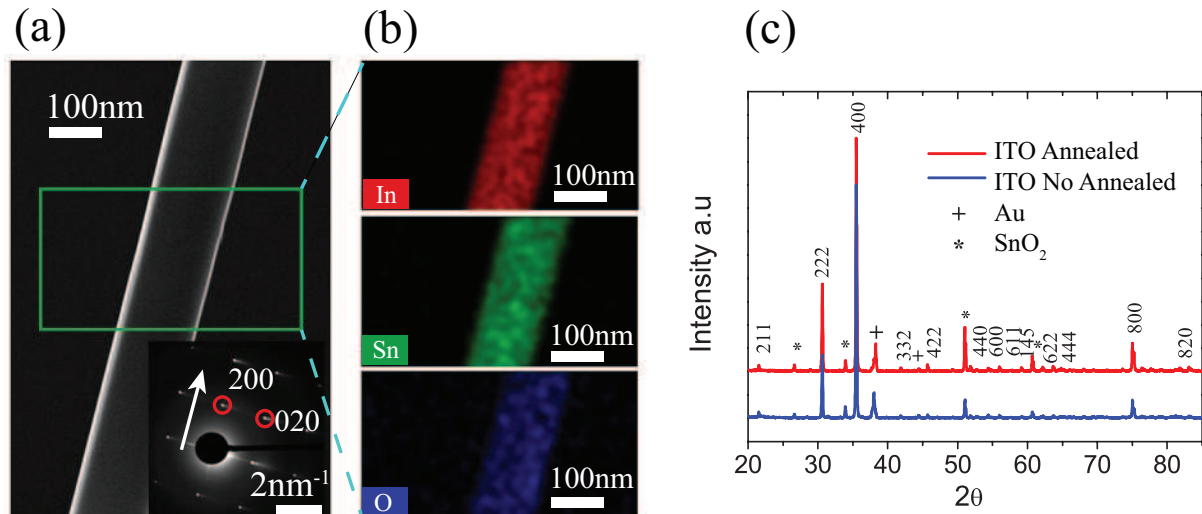


Figure 3.2: (a) SEM image, insert: SAED pattern for sample before annealing. (b) SEM-EDS mappings (c) XRD pattern for sample on substrate before and after 1300 °C annealing.

Indium, Tin and Oxygen concentrations were determined by analyzing quantitative EDS data from the measured nanowires. Figure 3.2 shows a SEM image 3.2(a), EDS

mapping 3.2(b), from where the chemical composition is obtained. EDS results are similar in the thermally treated samples up to 1300°C, see figure 3.3, 3.4 and table 3.1 for EDS maps and atomic percent estimates of all measured samples. XRD patterns, figure 3.2(c) shows all the main peaks corresponding to the  $\text{In}_2\text{O}_3$  cubic structure, indicating the incorporation of Sn into the  $\text{In}_2\text{O}_3$  lattice. Other small peaks are related to  $\text{SnO}_2$  and catalytic Au. The lattice parameter  $a$  calculated from XRD and SAED patterns are 10.1006 Å and 10.1003 Å, before and after annealing, respectively, confirming the thermal stability of the nanowires and discarding any obvious dislocation or clusters formation.

	Atomic % by element		
	In L	Sn K	O L
Sample 1	13.27	0.86	85.85
Sample 2	14.17	0.91	84.90
Sample 3	13.40	1.09	84.90
Annealed a	13.10	1.04	85.86
Annealed b	11.33	0.95	87.72
Annealed c	11.33	0.96	87.71

Table 3.1: Summary of atomic percent concentration approximation of measured ITO nanowires.

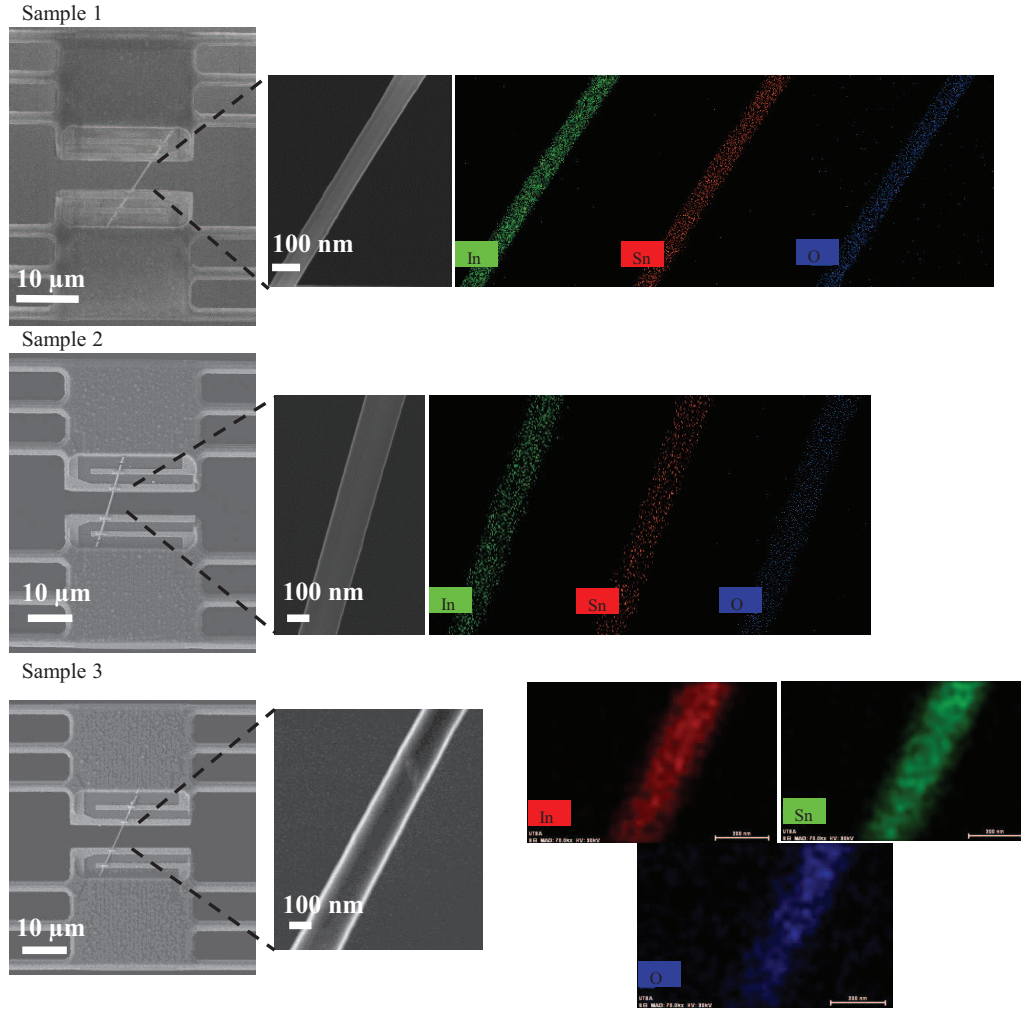


Figure 3.3: SEM images and EDS mapping for No annealing measures samples.

### 3.3 Thermoelectric Measurements and Discussion

After synthesis and heat treatment, annealed and nonannealed nanowires were detached from the substrates by sonication in 2-propanol and spread onto quartz substrates. After evaporation of the solvent, individual nanowires were selected, transferred by micromanipulation and finally mounted on specialized micro-devices for thermoelectric characterization. Figure 3.5 shows the SEM images of an ITO nanowire assembled onto a



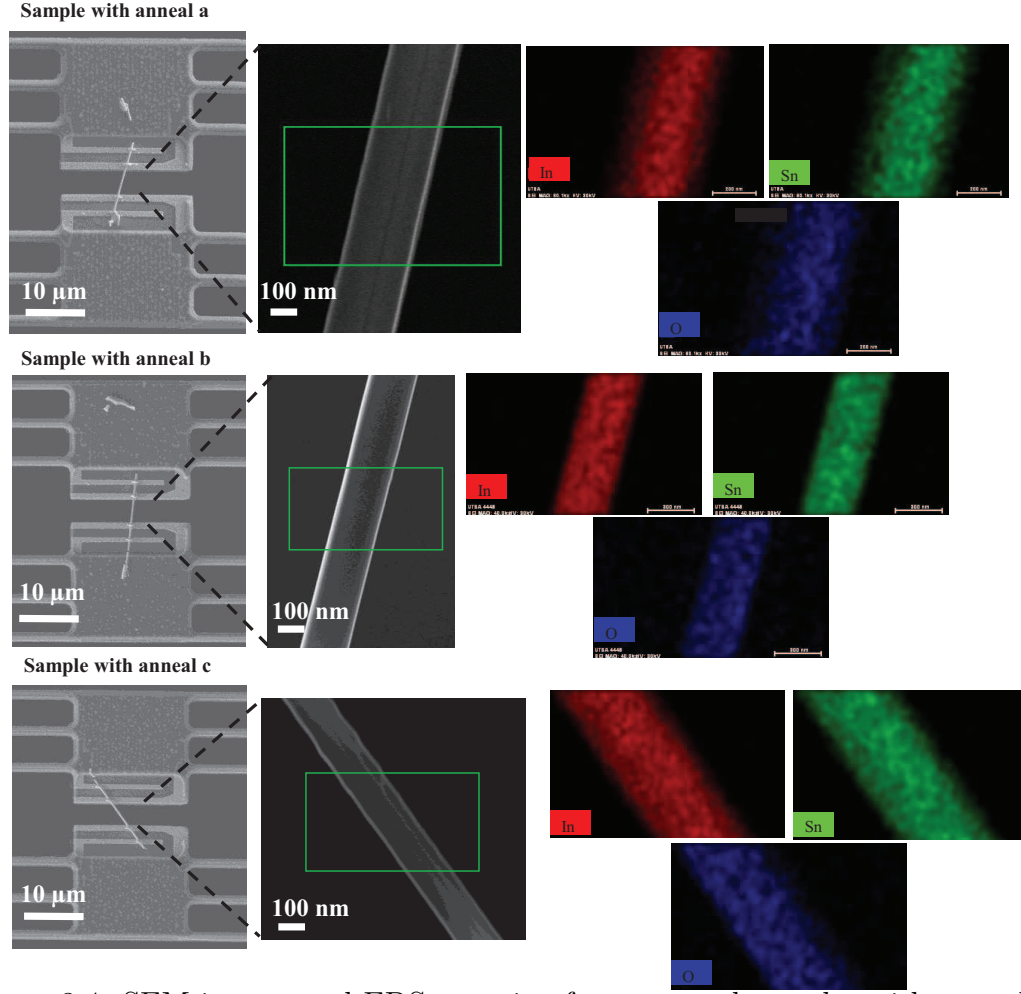


Figure 3.4: SEM images and EDS mapping for measured samples with annealing.

microdevice and connected to a four-electrode array. The device fabrication process and use is reported in earlier works [48-54]. Four Pt contacts were made in the nanowire using a focused ion beam (JEOL JEM9310) to electrically connect the nanowire to the device. For the measurements, the devices were finally attached to chip carriers and electrically connected using wire bonding. Thermoelectric measurements were performed on each nanowire over a 190-370 K temperature range.

Figure 3.6 summarizes the thermoelectric measurements. The temperature-dependent

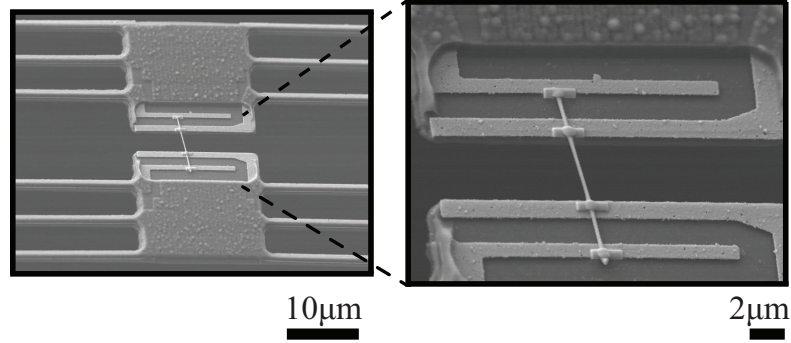


Figure 3.5: SEM images for a one single ITO nanowire onto specialized device.

Seebeck coefficient  $S$  is shown in Figure 3.6(a), the thermal  $\kappa$  and electrical  $\sigma$  conductivities are shown in Figure 3.6(b) and 3.6(c), respectively, and the figure of merit  $ZT$  is shown in Figure 3.6(d), all of which has been corrected to consider the thermal and electrical contact resistance of each nanowire-device ensemble. Thermal contact resistance is an important parameter in nanostructure materials, because in some cases it can dominate the thermal transport, especially in cases of weak bonding between the nanostructure and the substrate. In our samples the corrected thermal contact resistance was found about: 9% - 14% sample 1, 23% - 26% in sample 2, 15% - 25% in sample 3, 8% - 18% in annealed a, 17% - 25% in annealed b and 7% - 16% in annealed 3 of the total thermal resistance [48]

The negative values of  $S$  confirm the expected  $n$ -type behavior. The absolute value of the Seebeck coefficient increases almost linearly with temperature in all studied samples, with a greater slope and values for thermally treated ones. Wu et. al. [40] and Li et. al. [38] found a similar behavior in ITO thin films with annealing temperatures between 150 and 450 °C. The lowest total thermal conductivity values for the ITO nanowires

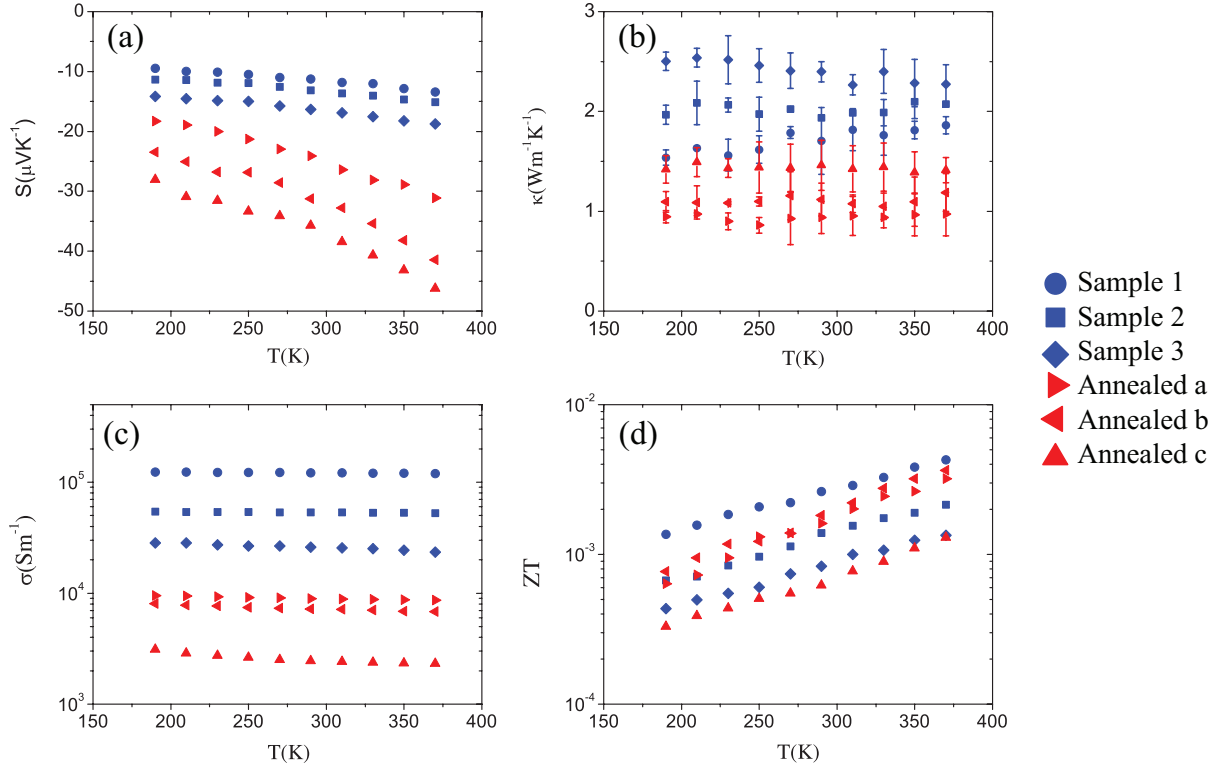


Figure 3.6: (a) Measured Seebeck coefficient  $S$ , (b) Thermal Conductivity ( $\kappa$ ), electrical conductivity ( $\sigma$ ) and (d)  $ZT$  as a function of Temperature of ITO nanowires.

was between  $\sim 1$  and  $\sim 1.5 \text{ Wm}^{-1}\text{K}^{-1}$  corresponding to the annealed samples (Figure 3.6(b)), staying practically constant in the studied temperature range. In the case of non-annealed samples, the thermal conductivity was between  $\sim 1.8$  and  $\sim 2.6 \text{ Wm}^{-1}\text{K}^{-1}$ . The decrease of the total thermal conductivity in annealed samples can be attributed mainly to the reduced contribution of electronic thermal conductivity as will be discussed. These values are lower than the reported thermal conductivity for  $\text{In}_2\text{O}_3$ -based compounds (2.0-8.5  $\text{Wm}^{-1}\text{K}^{-1}$  for different doping) [43-45]

The temperature dependence of the electrical conductivity is dominated by the free carriers and decreases as the temperature increases, similarly to previous reports in thin

films [38,39,41,55] and nanowires [11,17,19]. Thermally treated samples show almost an order of magnitude lower electrical conductivity that is consistent with our observation of a large increase in  $S$  for all annealed samples, and a lowering of the carrier concentration due to reduction of oxygen vacancy sites as evidenced from the EDS results. The thermoelectric performance of the ITO nanowires is shown in Figure 3.6d. The  $ZT$  value have a maximum of  $4.28 \times 10^{-3}$  at 370 K in sample 1, and similar values were obtained in annealed samples with a maximum of  $3.64 \times 10^{-3}$  in the annealed b sample.

The total thermal conductivity  $\kappa$  can be separated into two terms, one is the contribution from the free charges and the other from the lattice vibrations, and expressed as,  $\kappa = \kappa_e + \kappa_L$  where  $\kappa_e$  is the electronic thermal conductivity and  $\kappa_L$  is the lattice thermal conductivity. The electronic contribution (Figure 3.7(a)) was estimated according to the Wiedemann-Franz Law ( $\kappa_e = \sigma LT$ ), where  $T$  refers to the absolute temperature and  $L$  is the Lorentz number. In the Sommerfeld limit of a free electron gas  $L$  can be derived as  $L_0 = \pi^2 k_B^2 / (3e^2) = 2.44 \times 10^{-8} \text{ W}\Omega\text{K}^{-2}$  where  $k_B$  is the Boltzmann constant and  $e$  is the elementary electron charge [56,57]. The lattice contribution was calculated from the difference between the measured total thermal conductivity and  $\kappa_e$  assuming  $L_0$  and is shown in Figure 3.7b. We note that  $L_0$  is the metallic limit of  $L$ , and for semiconductors an empirical expression has been developed for the non-degenerate regime as a function of Seebeck coefficient [58]  $L = 1.5 \times 10^{-8} + \exp\left(\frac{|S|}{116}\right) \times 10^{-6}$ . We note that in the limit of our measured Seebeck coefficients,  $L$  is  $\sim 2.35 - 2.42 \times 10^{-8} \text{ W}\Omega\text{K}^{-2}$ , for the as-grown samples and  $\sim 2.17 - 2.36 \times 10^{-8} \text{ W}\Omega\text{K}^{-2}$  for the annealed samples.

Thus by assuming  $L_0$ , the maximum uncertainty error propagated to  $\kappa_L$  is expected to be a 0.6 – 3.43% overestimation for the as-grown samples, and a 3.4-11.2% overestimation for the annealed samples according to Hyun et. al. [58]. Thus,  $\kappa_L$  and  $ZT$  values here reported may be slightly overestimated and slightly underestimated, respectively. As expected, phonons were the main contributors to the thermal transport. Detailed modeling of  $\hat{\kappa}_L$  was used to obtain more information about defect formation during the thermal treatment, where  $\kappa_L$  was calculated in terms of the dislocations and impurity density using a modified Debye-Callaway model [59] which also takes into account the contributions from umklapp processes and boundary phonon scattering [60-62].

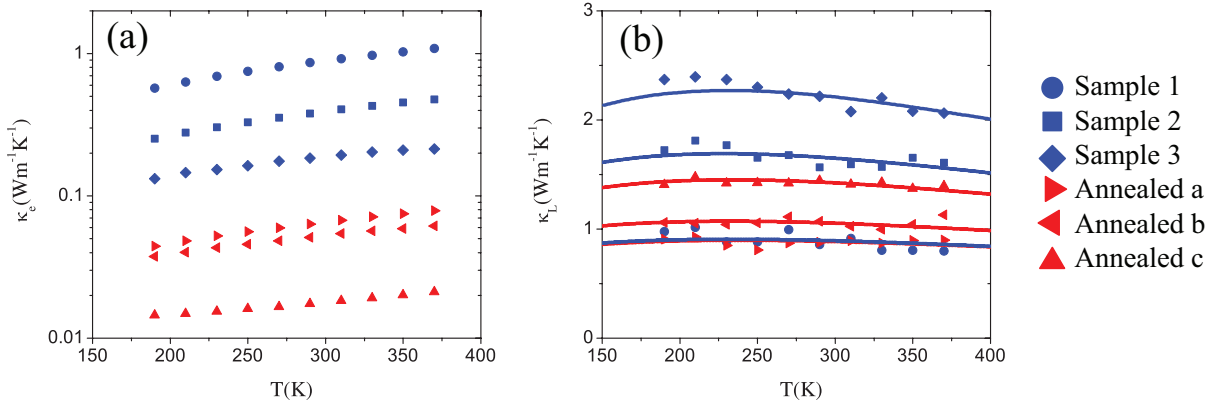


Figure 3.7: (a) Electron thermal conductivity. (b) Lattice thermal conductivity as function of temperature. The continue lines are the model fittings.

In the modified Debye-Callaway model,  $\kappa_{ph}(T)$  can be expressed as:

$$\kappa_{ph}(T) = \frac{K_B}{2\pi v_s} \left( \frac{K_B T}{\hbar} \right)^3 \int_0^{T_D/T} \frac{x^4 e^x}{\tau_{ph}^{-1} (e^x - 1)^2} dx \quad (3.1)$$

with

$$\tau_{ph}^{-1} = \tau_I^{-1} = \tau_D^{-1} = \tau_U^{-1} = \tau_B^{-1} + \dots = A\alpha^4 T^4 x^4 + RTx + B\alpha^2 T^3 x^3 e^{-T_D/T} + \frac{v_s}{D} + \dots \quad (3.2)$$

Where  $x = \frac{\hbar\omega}{K_B T}$  is the reduced phonon frequency,  $\hbar$  is the reduced Planck constant,  $K_B$  is the Boltzmann constant,  $v_s = 6400$  m/s is the speed of sound,  $T_D = 700$  K is the Debye temperature [60] and  $T$  is the absolute temperature. The fitting parameters are:  $A$  for point defects,  $R$  for dislocations, and  $B$  for the umklapp processes. Parameter  $D$  is related to the scattering at the boundaries and in our case identified as the diameter of the nanowires.  $D$  was obtained from the electron microscopy inspection of each sample. The best fitting of the observed  $\kappa_L$  values gave  $R$  and  $B$  parameters practically unchanged for all the samples, with assigned values of  $1 \times 10^9 \text{ s}^{-1} \text{ K}^{-1}$  and  $8 \times 10^{-18} \text{ sK}^{-1}$ , respectively. The values for  $A$  and  $D$  used for each sample are summarized in table 3.2. Figure 5b includes the results from the model calculations as continue lines. The comparison in Table 3.2 between the values of impurities ( $A$ ) before and after 1300°C thermal treatment shows an overall increase of point defects contribution during annealing, but within the same order of magnitude.

The comparison between the results from XRD, EDS, electrical and thermal transport between as-grown samples and 1300°C heat treated samples confirms high overall thermal stability of ITO nanowires with diameters in the 180-330 nm range that suggests applicability of these nanostructures to work in high temperatures in an expanded area

Sample	$A \times 10^{-41} (s^3)$	D(nm)
Sample 1	1.25	230
Sample 2	0.48	320
Sample 3	0.27	180
Sample a	1.30	330
Sample b	1.00	330
Sample c	0.58	220

Table 3.2: Values of impurities (A) and boundary (D) parameters used in the modified Debye-Callaway model given by equation 3.1.

of applications that includes thermoelectricity. The combination of increased Seebeck coefficients and reduced electrical conductivities after annealing suggests a reduction in the charge carrier density that is compatible with the change in defect density. From the point of view of thermoelectrical power generation, the increased  $S$  and reduced  $\kappa$  and  $\sigma$  work against each other to finally produce little overall changes in  $ZT$  upon thermal annealing.

## 3.4 Conclusions

The Seebeck coefficient, the thermal and the electrical conductivities were successfully measured to obtain the thermoelectric figure of merit of individual single crystalline ITO

---

nanowires with and without 30 minutes of thermal treatment in air at temperatures up to 1300°C. ITO nanowires were synthesized by a VLS process with diameters in the 180-330 nm range. The comparison between the samples response with and without annealing showed relatively high thermal tolerance of the material at the nanoscale that encourages its use in applications designed to operate at high temperatures up to 1300°C. In particular, the thermoelectric response of the studied ITO nanowires makes them a promising candidate as  $n$ -type thermoelectric building block to develop nanodevices to operate in harsh environments.



## 3.5 References

- [1] Bierwagen, O., Indium oxide—A transparent, wide-band gap semiconductor for (opto)electronic applications. *Semiconductor Science and Technology*, 2015. 30(2): p. 024001-1-.
- [2] Yang, J., A. Banerjee, and S. Guha, Triple-junction amorphous silicon alloy solar cell with 14.6% initial and 13.0% stable conversion efficiencies. *Applied Physics Letters*, 1997. 70(22): p. 2975-2977.
- [3] Günes, S., H. Neugebauer, and N.S. Sariciftci, Conjugated polymer-based organic solar cells. *Chemical reviews*, 2007. 107(4): p. 1324-1338.
- [4] Huynh, W.U., J.J. Dittmer, and A.P. Alivisatos, Hybrid nanorod-polymer solar cells. *science*, 2002. 295(5564): p. 2425-2427.
- [5] Yu, H.K., et al., Three-dimensional nanobranched indium-tin-oxide anode for organic solar cells. *ACS nano*, 2011. 5(10): p. 8026-8032.
- [6] Kee, Y.Y., et al., Low-temperature synthesis of indium tin oxide nanowires as the transparent electrodes for organic light emitting devices. *Nanotechnology*, 2012. 23(2): p. 025706.
- [7] O'Dwyer, C., et al., Bottom-up growth of fully transparent contact layers of indium tin oxide nanowires for light-emitting devices. *Nat Nanotechnol*, 2009. 4(4): p. 239-44.

- 
- [8] Patel, N., P. Patel, and V. Vaishnav, Indium tin oxide (ITO) thin film gas sensor for detection of methanol at room temperature. *Sensors and Actuators B: Chemical*, 2003. 96(1-2): p. 180-189.
  - [9] Baetens, R., B.P. Jelle, and A. Gustavsen, Properties, requirements and possibilities of smart windows for dynamic daylight and solar energy control in buildings: A state-of-the-art review. *Solar Energy Materials and Solar Cells*, 2010. 94(2): p. 87-105.
  - [10] Orlandi, M.O., et al., Tin-doped indium oxide nanobelts grown by carbothermal reduction method. *Applied Physics A*, 2005. 80(1): p. 23-25.
  - [11] Gao, J., et al., UV light emitting transparent conducting tin-doped indium oxide (ITO) nanowires. *Nanotechnology*, 2011. 22(19): p. 195706.
  - [12] Chiquito, A.J., et al., Electron dephasing and weak localization in Sn doped  $\text{In}_2\text{O}_3$  nanowires. *Nano letters*, 2007. 7(5): p. 1439-1443.
  - [13] Berengue, O.M., et al., Structural characterization of indium oxide nanostructures: a Raman analysis. *Journal of Physics D: Applied Physics*, 2010. 43(4): p. 045401.
  - [14] Gao, J., et al., Phase selection enabled formation of abrupt axial heterojunctions in branched oxide nanowires. *Nano letters*, 2011. 12(1): p. 275-280.
  - [15] Nguyen, P., et. al., Epitaxial directional growth of indium-doped tin oxide nanowire arrays. *Nano Letters*, 2003. 3(7): p. 925-928.

- 
- [16] Meng, G., et al., A flux induced crystal phase transition in the vapor-liquid-solid growth of indium-tin oxide nanowires. *Nanoscale*, 2014. 6(12): p. 7033-7038.
- [17] Meng, G., et al., Impact of Preferential Indium Nucleation on Electrical Conductivity of Vapor-Liquid-Solid Grown Indium-Tin Oxide Nanowires. *Journal of the American Chemical Society*, 2013. 135(18): p. 7033-7038.
- [18] Park, K.S., et al., The effect of the concentration and oxidation state of Sn on the structural and electrical properties of indium tin oxide nanowires. *Nanotechnology*, 2011. 22(28): p. 285712.
- [19] Chiu, S.-P., et al., Four-probe electrical-transport measurements on single indium tin oxide nanowires between 1.5 and 300 K. *Nanotechnology*, 2009. 20(10): p. 105203.
- [20] Wan, N., et al., Broadband anti-reflection and enhanced field emission from catalyst-free grown small-sized ITO nanowires at a low temperature. *Acta Materialia*, 2010. 58(8): p. 3068-3072.
- [21] Yu, D., et al., Synthesis of ITO nanowires and nanorods with corundum structure by a co-precipitation-anneal method. *Materials Letters*, 2004. 58(1): p. 84-87.
- [22] Lin, D., et al., Preparation and electrical properties of electrospun tin-doped indium oxide nanowires. *Nanotechnology*, 2007. 18(46): p. 465301.
- [23] Fung, M., et al., Indium tin oxide nanowires growth by dc sputtering. *Applied*

- Physics A, 2011. 104(4): p. 1075-1080.
- [24] Kovtyukhova, N.I. and T.E. Mallouk, Conductive indium-tin oxide nanowire and nanotube arrays made by electrochemically assisted deposition in template membranes: switching between wire and tube growth modes by surface chemical modification of the template. *Nanoscale*, 2011. 3(4): p. 1541-1552.
- [25] Bell, L.E., Cooling, heating, generating power, and recovering waste heat with thermoelectric systems. *Science*, 2008. 321(5895): p. 1457-1461.
- [26] Fergus, J.W., Oxide materials for high temperature thermoelectric energy conversion. *Journal of the European Ceramic Society*, 2012. 32(3): p. 525-540.
- [27] Zhao, D. and G. Tan, A review of thermoelectric cooling: materials, modeling and applications. *Applied Thermal Engineering*, 2014. 66(1): p. 15-24.
- [28] Zhang, X. and L.-D. Zhao, Thermoelectric materials: Energy conversion between heat and electricity. *Journal of Materiomics*, 2015. 1(2): p. 92-105.
- [29] He, J. and T.M. Tritt, Advances in thermoelectric materials research: Looking back and moving forward. *Science*, 2017. 357(6358): p. 1369 & eaak9997-1â&#x2013;9.
- [30] Hicks, L. and M. Dresselhaus, Effect of quantum-well structures on the thermoelectric figure of merit. *Physical Review B*, 1993. 47(19): p. 12727.
- [31] Dresselhaus, M.S., et al., New Directions for Lowâ&#x2013;Dimensional Thermoelectric Materials. *Advanced Materials*, 2007. 19(8): p. 1043-1053.

- 
- [32] Li, J.-F., et al., High-performance nanostructured thermoelectric materials. *NPG Asia Mater*, 2010. 2: p. 152-158.
- [33] Nielsch, K., et al., Thermoelectric nanostructures: from physical model systems towards nanograined composites. *Advanced Energy Materials*, 2011. 1(5): p. 713-731.
- [34] Heremans, J.P., et al., When thermoelectrics reached the nanoscale. *Nat Nano*, 2013. 8(7): p. 471-473.
- [35] Koumoto, K., et al., Oxide thermoelectric materials: a nanostructuring approach. *Annual Review of Materials Research*, 2010. 40: p. 363-394.
- [36] Walia, S., et al., Transition metal oxides-Thermoelectric properties. *Progress in Materials Science*, 2013. 58(8): p. 1443-1489.
- [37] Ren, G., et al., High performance oxides-based thermoelectric materials. *JOM*, 2015. 67(1): p. 211-221.
- [38] Li, Z. and J.-J. Lin, Electrical resistivities and thermopowers of transparent Sn-doped indium oxide films. *Journal of applied physics*, 2004. 96(10): p. 5918-5920.
- [39] Lin, B.-T., et al., Temperature dependence of resistance and thermopower of thin indium tin oxide films. *Thin Solid Films*, 2010. 518(23): p. 6997-7001.
- [40] Wu, C.-Y., et al., Free-electronlike diffusive thermopower of indium tin oxide thin films. *Journal of Applied Physics*, 2010. 108(12).

- 
- [41] El Amrani, A., et al., Electronic transport and optical properties of thin oxide films. *Thin Solid Films*, 2010. 518(16): p. 4582-4585.
- [42] Guilmeau, E., et al., Tuning the transport and thermoelectric properties of  $\text{In}_2\text{O}_3$  bulk ceramics through doping at In-site. *J. Appl. Phys*, 2009. 106(5): p. 053715.
- [43] Zhu, B., et al., Enhancement of thermoelectric properties in Sn doped  $(\text{In}_{0.95}\text{Lu}_{0.05})_2\text{O}_3$ . *Journal of Alloys and Compounds*, 2015. 644: p. 119-123.
- [44] Liu, Y., et al., Effect of Transition Metal Cobalt Doping on the Thermoelectric Performance of  $\text{In}_2\text{O}_3$  Ceramics. *Journal of the American Ceramic Society*, 2010. 93(10): p. 2938-2941.
- [45] Liu, Y., et al., Thermoelectric Performance of Zn and Nd Co-doped  $\text{In}_2\text{O}_3$  Ceramics. *Journal of electronic materials*, 2011. 40(5): p. 1083-1086.
- [46] Combe, E., et al., Microwave sintering of Ge-doped  $\text{In}_2\text{O}_3$  thermoelectric ceramics prepared by slip casting process. *Journal of the European Ceramic Society*, 2015. 35(1): p. 145-151.
- [47] Liu, Y., et al., Enhanced thermoelectric properties of G-doped  $\text{In}_2\text{O}_3$  ceramics via synergistic band gap engineering and phonon suppression. *Physical Chemistry Chemical Physics*, 2015. 17(17): p. 11229-11233.
- [48] Mavrokefalos, A., et al., Four-probe measurements of the in-plane thermoelectric properties of nanofilms. *Review of scientific instruments*, 2007. 78(3): p. 034901.

- 
- [49] Pettes, M.T. and L. Shi, Thermal and Structural Characterizations of Individual Single-, Double-, and Multi-Walled Carbon Nanotubes. *Advanced Functional Materials*, 2009. 19(24): p. 3918-3925.
- [50] Shi, L., et al., Measuring thermal and thermoelectric properties of one-dimensional nanostructures using a microfabricated device. *Journal of heat transfer*, 2003. 125(5): p. 881-888.
- [51] Zhou, F., et al., Determination of transport properties in chromium disilicide nanowires via combined thermoelectric and structural characterizations. *Nano letters*, 2007. 7(6): p. 1649-1654.
- [52] Hsu, I.-K., et al., Optical absorption and thermal transport of individual suspended carbon nanotube bundles. *Nano letters*, 2009. 9(2): p. 590-594.
- [53] Zhou, F., et al., Effect of growth base pressure on the thermoelectric properties of indium antimonide nanowires. *Journal of Physics D: Applied Physics*, 2010. 43(2): p. 025406.
- [54] Valentín, L., et al., A comprehensive study of thermoelectric and transport properties of Îš-silicon carbide nanowires. *Journal of Applied Physics*, 2013. 114(18): p. 184301.
- [55] Brinzari, V., et al., Thermoelectrical properties of spray pyrolyzed indium oxide thin films doped by tin. *Thin Solid Films*, 2014. 552: p. 225-231.

- 
- [56] Kittel, C., Introduction to Solid State Physics. 8th ed. 2005, New York: John Wiley & Sons.
- [57] Dmitriev, A.V. and I.P. Zvyagin, Current trends in the physics of thermoelectric materials. Physics-Uspekhi, 2010. 53(8): p. 789-803.
- [58] Kim, H.-S., et al., Characterization of Lorenz number with Seebeck coefficient measurement. APL Materials, 2015. 3(4): p. 041506-1â€Œ5.
- [59] Callaway, J., Model for lattice thermal conductivity at low temperatures. Physical Review, 1959. 113(4): p. 1046.
- [60] Kinemuchi, Y., et al., Tuning of dimensionless figure of merit via boundary scattering in In<sub>2</sub>O<sub>3</sub>. Journal of Applied Physics, 2011. 110(12): p. 124304.
- [61] Pei, Y., et al., Convergence of electronic bands for high performance bulk thermoelectrics. Nature, 2011. 473(7345): p. 66-69.
- [62] Ortiz, B.R., et al., Effect of extended strain fields on point defect phonon scattering in thermoelectric materials. Physical Chemistry Chemical Physics, 2015. 17(29): p. 19410-19423.



# Chapter 4

## Thermoelectric Properties of SnSe Nanowires with different diameters

---

### 4.1 Introduction

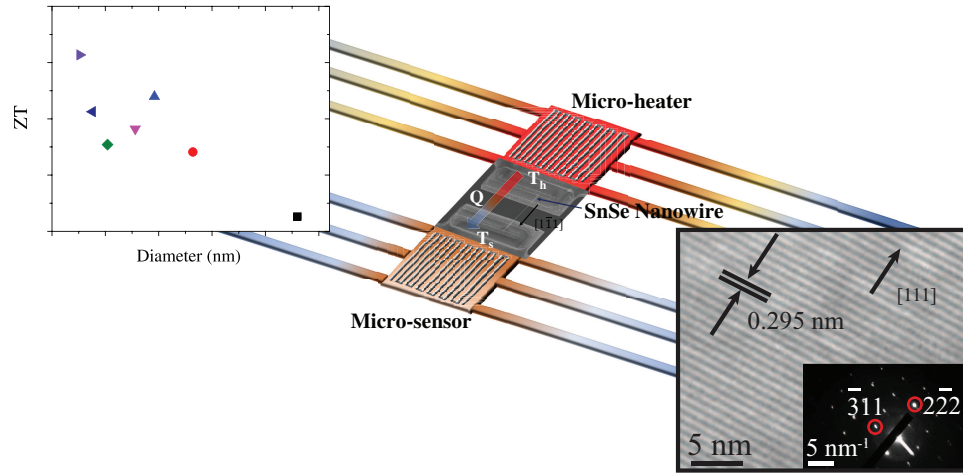


Figure 4.1: Summary art concept of SnSe study

In 2014 Zhao et al. [1] reported a record figure of merit,  $ZT \sim 2.6$  at 923 K along the  $b$ -axis of single crystalline SnSe. This chalcogenide material adds an extra advantage in its composition, it is lead free and shows ultralow lattice thermal conductivity due to its layered structure, with atoms arranged similarly to a highly distorted rock salt structure,

where the bonding of SnSe interacts covalently within the layers and forms anharmonic and anisotropic bonding; [2,3] along the efforts to optimize this efficiency, highly doped *p*-type SnSe materials has been studied but their increasing charge density leads to a decrease in the Seebeck coefficient and in the figure of merit, with a maximum value of  $ZT = 0.6$  reported at 1023K with Ag-doping [4], 2.0 in hole-doped crystals at 773K [5] and below 1 for Pb, Cu, Al, In and Ag doping [6] at  $T > 750$ K. Many theoretical calculations have been carried out to describe the relationship between structural, electronic, phononic and thermoelectric properties in orthorhombic materials, and specially in *n*- and *p*-type SnSe [7-12] and in single monolayers [13]. Calculations suggest the possibility of a high thermoelectric figure of merit in nanostructured SnSe crystals [14] that motivated this study on the diameter dependence of the thermoelectric performance of SnSe nanowires.

## 4.2 Experimental Results, calculations and Discussion

The synthesis of the SnSe nanowires was carried out using a catalyst-assisted thermal vapor-liquid-solid (VLS) process, similar to the procedure used by Butt et al. [15], in which high purity powders of Tin (99.998% purity, Sigma-Aldrich) and Selenium (99.995%, Sigma-Aldrich) were used as source materials. The mixed powders were loaded

on alumina boats and positioned at the center of the first hot zone of a two-zones horizontal quartz tube furnace (MTI 1200X). Several sapphire substrates coated with a thin Au film with thickness between 1-3 nm, were located in the middle of an alumina boat positioned between both heating zones. The furnace was heated to 860 °C and 550 °C in the precursor and substrate zone respectively, at a rate of 10 °C min<sup>-1</sup> and the temperature was then maintained constant for 60 min, before natural cooling to room temperature. During the synthesis the system was kept at atmospheric pressure, using 100 sccm of Ar as the carrier gas.

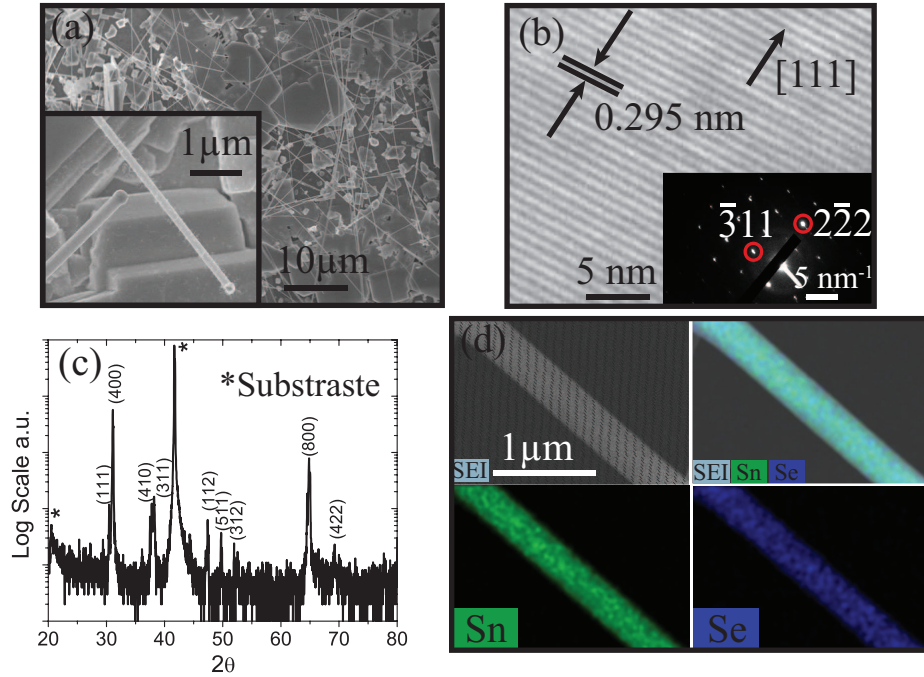


Figure 4.2: (a) SEM image of the as-grown SnSe nanowires. (b) HRTEM and SAED for a measured SnSe NW (1.15  $\mu\text{m}$ ). (c) XRD pattern, (\* corresponds to the sapphire substrate). (d) SEM EDS mapping for a measured SnSe nanowire (480 nm).

The SnSe nanowires were formed uniformly on the surface of the substrates, with

different diameters and several tens of microns in length. Figure 4.2a shows the SEM image of as deposited nanowires. The higher magnification inset shows a typical nanowire grew from a SnSe seed crystal using Au as the catalyst. HRTEM data (figure 1b) shows high crystalline order at the scale of the image of the measured nanowires and gives an interplanar spacing value of 2.95 Å corresponding to the array of planes perpendicular to the nanowire axis consistent with a SnSe crystal growth along the [111] direction.

This information is supported by selected area electron diffraction and X-ray diffraction (XRD) patterns that confirm the formation of orthorhombic phase (Pnma) with lattice parameters:  $a = 11.46$ ,  $b = 4.14$  and  $c = 4.38$  Å,  $\alpha = \beta = \gamma = 90^\circ$ . XRD (figure 1c) shows only SnSe patterns without any evidence of crystalline SnO, SnO<sub>2</sub>, SnSe<sub>2</sub> or Sn and Se byproducts. Quantified data from HRSEM-EDS is consistent with an approximate 1:1 Sn:Se ratio and compositional uniformity, a slightly reduced Sn signal could be evidence of native Sn vacancies in our *p*-type samples. The EDS spectra and quantification is given in figure 4.3.

After synthesis, the nanowires were detached from the substrates by sonication in ethanol and dispersed on a Si substrate for inspection and micromanipulation. Nanowires with different diameters were selected and transported to suspended microdevices to measure  $S$ ,  $\sigma$  and  $\kappa$ , according to the procedure detailed in previous studies [16-19]. Using a high magnification optical microscope (Nikon Eclipse E600), the selected nanowire was then attached to the tip by van der Waals forces, moved to the device and aligned properly

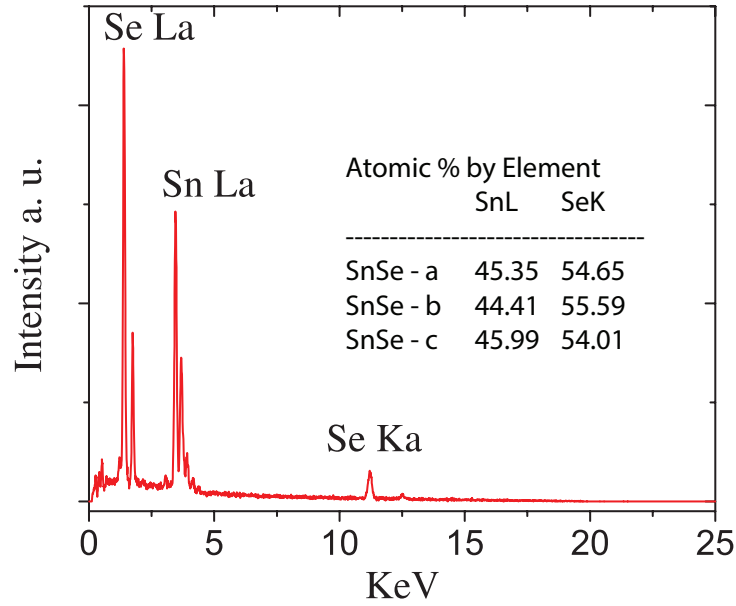


Figure 4.3: SEM - EDS spectra for 3 SnSe nanowire samples. The inset shows the atomic ratio for Sn and Se.

to let the nanowire contact the four Pt electrodes. Once the nanowire was in place, a focused ion beam system (Jeol JEM 9310 FIB) was used to remove possible contaminants from the surface of the nanowire and to deposit Pt at the contact sites. The measuring device with the integrated nanowire was then wirebonded (Kulicke & Soffa 4524) to a chip carrier in order to connect it to the measurement setup.

The prepared samples were placed in a cryostat chamber, pumped with a turbomolecular pump to reduce pressure to  $\sim 5 \times 10^{-6}$  Torr to minimize convection heat losses. Using two locking amplifiers, a DC source, two voltages and one current amplifiers, a thermal gradient were created between the ends of the nanowire and the voltage drop was measured between the inner and outer contact electrodes, respectively. The temperatures at

the ends and the two thermoelectric voltages were measured for different ambient temperatures between 150 K and 370 K using liquid Nitrogen and a temperature controller. From these measurements the contact thermal resistance, corrected thermal conductivity, the Seebeck coefficient, and the electrical conductivity of each nanowire were obtained.

Figure 4.4 shows SEM images for 7 measured nano- and micro-wires.

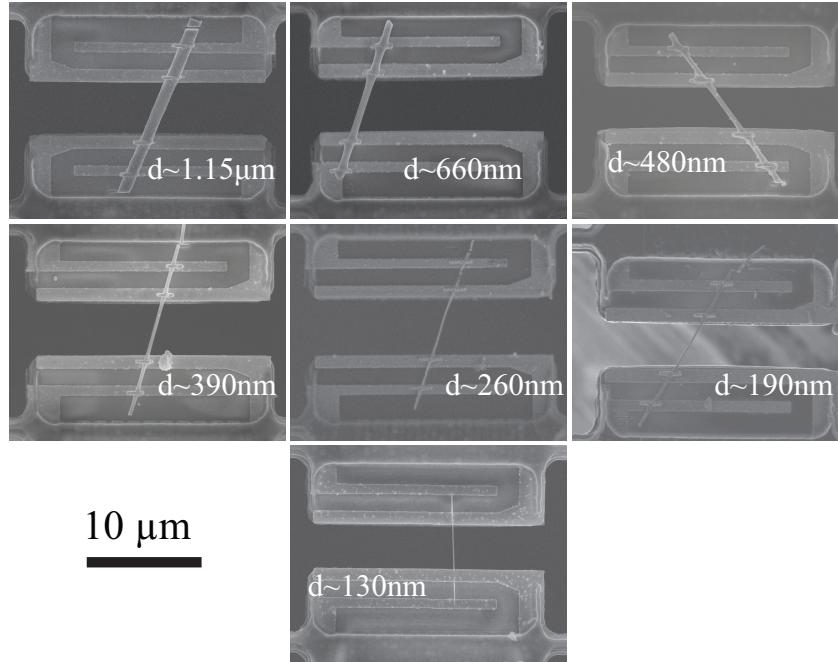


Figure 4.4: SEM images of SnSe nanowires aligned on specialized micro devices for diameters between  $1.15 \mu\text{m}$  to 130 nm.

Figure 4.5 shows a close-up SEM image of a typical SnSe nanowire integrated to the measuring microdevices. A Focus Ion Beam system (JEOL JEM9310 FIB) was used to remove possible contaminants from the surface of the nanowire at the nanowire/electrode regions, and to deposit Pt at these sites in order to establish a good electrical

contact. The possible defect formation due to  $\text{Ga}^+$  ion bombardment during FIB deposition was kept to a minimum by avoiding unnecessary  $\text{Ga}^+$  beam irradiation of the entire nanowire but it cannot be excluded completely. After the transport measurements, each nanowire was observed via SEM and TEM to determine diameters and lengths among the electrodes such that conductivities could be obtained from the corresponding measured conductances.

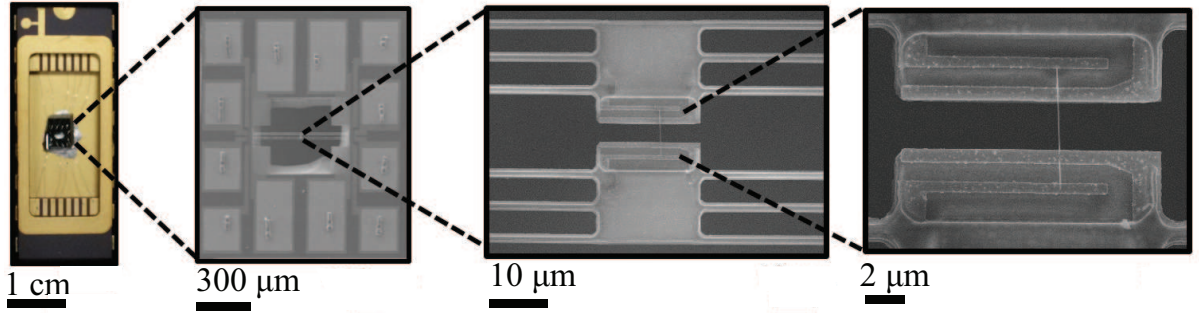


Figure 4.5: From left to right, optical image of the micro-thermometry device wired to a chip carrier, followed by low and high magnification SEM images of a 130 nm nanowire transferred onto the micro-device.

The measured Seebeck coefficient, the thermal conductivity, the electrical conductivity, and the calculated figure of merit as a function of temperature of nanowires with different diameters are shown in figure 4.6. In all cases the measured  $S$  was positive indicating  $p$ -type transport, increased in magnitude with increasing temperature, and did not show a clear diameter dependence. These results are in overall agreement with the study by Zhao et. al. in bulk SnSe and SnSe doped crystals [1,5]. Singh et al.[6] and Sassi et al. [19] in bulk polycrystalline samples, and with the studies in SnSe nanostructured sheets by Serrano-Sanchez et al.[20] Figure 4.6b confirms ultralow thermal conductivities

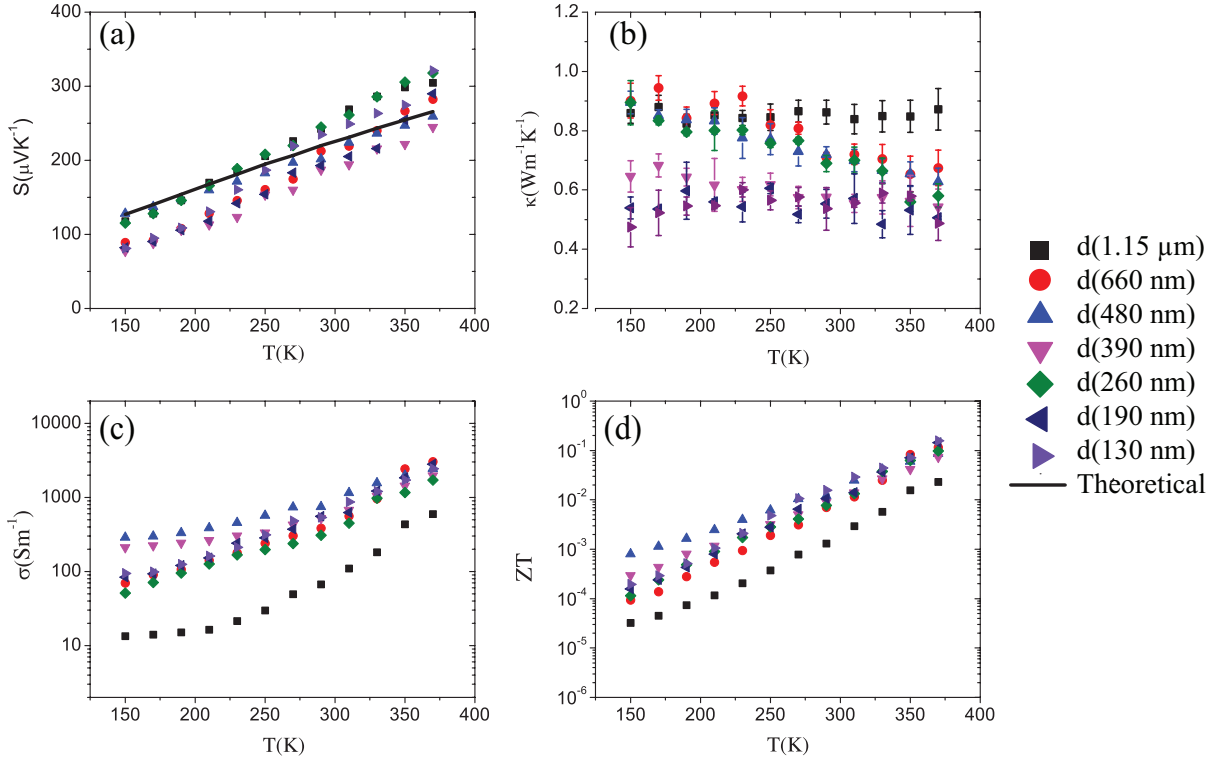


Figure 4.6: (a) Measured Seebeck coefficient  $S$ , (b) thermal conductivity  $\kappa$ , (c) electrical conductivity  $\sigma$  and (d)  $ZT$  of SnSe nanowires with different diameters as a function of temperature.

for all nanowires and in the same order of the reported values for bulk samples.[1,5,21]  $\kappa$  values were corrected to consider the thermal contact resistance of the measuring device. A significant reduction in  $\kappa$  is observed in the samples with smaller diameters. In the thicker nanowires  $\kappa$  slightly decreases when the temperature is increased as found in bulk samples by Zhao et al.,[1] for smaller diameters (130 nm, 190 nm and 390 nm) the thermal conductivity remains practically constant or with a small increase with temperature in the 130 nm wire. This behavior is consistent with the increasing contribution of phonons



surface scattering in thin nanowires,[17,22,23] in contrast to a recent thermal conductivity accumulation study by Guo et al. [14] found negligible contribution of phonons with wavelengths above  $\sim 100$  nm to the lattice thermal conductivity. Thus, both the temperature dependence of the thermal conductivity and the magnitude indicate static scattering processes are considerable in the samples of this work. From Guo et al. [14] work, we should expect that anharmonic processes will dominate in nanowires of the diameters considered here. The  $d = 1.15 \mu\text{m}$  sample shows reduced temperature dependence in the measured temperature range and significantly lower electrical conductivity when compared with other samples, suggesting a higher density of crystal defects in this particular nanowire.

The electrical resistance measurements were performed in a four-point configuration and the electrical conductivity was calculated after the determination by TEM and SEM of each nanowires length and diameter, see figure 4.4 and figure 4.7 where the cross section suggests rounded shape. Figure 4.6(c) shows that  $\sigma$  is thermally activated in all samples within the measured temperature range as has been reported for polycrystalline SnSe [4,6,20,24] and consistent with unintentional  $p$ -doping of the nanowires attributed to native Sn vacancies that act as double acceptors. Figure 4.6(c) shows variations of  $\sigma$  between samples at low temperature ( $T \sim 150\text{K}$ ) with no clear dependence on diameter but at higher temperatures these differences become less significant, reaching values in the order of 1000 S/m at room temperature, consistent with reports in bulk polycrystalline samples [4,6,21]. Finally, the figure of merit ( $ZT$ ) was calculated from the measured  $S$ ,  $\kappa$

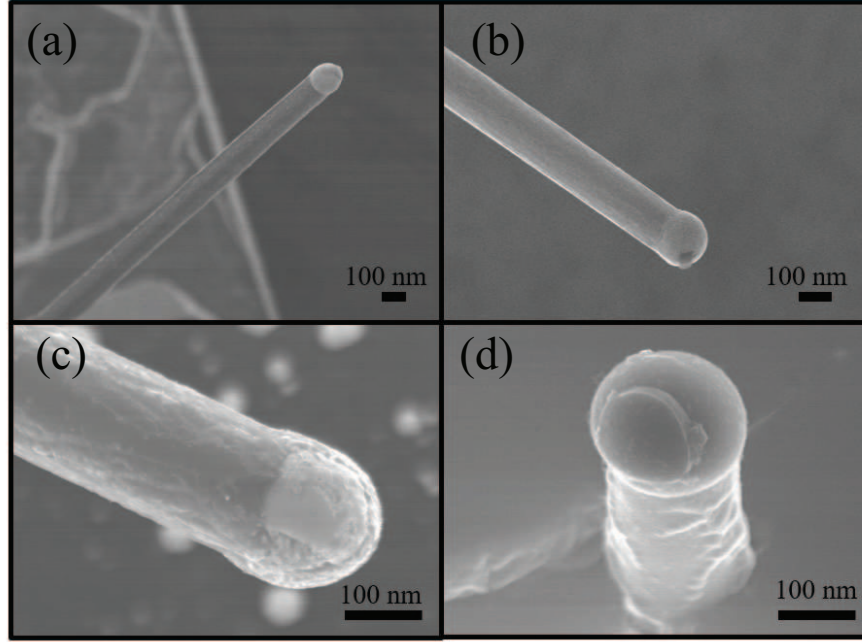


Figure 4.7: SEM images of the growth nanowire on substrate. The cross section suggests rounded shape.

and  $\sigma$  as a function of temperature. Figure 4.6(d) shows increasing  $ZT$  for all nanowires as the temperature is increased. The maximum measured  $ZT$  was 0.156 corresponding to the thinner nanowire at 370 K, well above than what is reported in unintentionally doped polycrystalline bulk samples [4,6,21].

In order to gain insight into the effects of the reducing nanowire diameter on the thermal conductivity and  $ZT$ , figure 4.8 shows the thermal conductivity and the figure of merit close to room temperature (290 K) as a function of the nanowire diameter, respectively. Figure 4.8(a) (dots) shows an overall decrease of the thermal conductivity with decreasing diameter attributed to a reduced averaged phonon mean free path with  $\kappa \sim 0.55 \text{ Wm}^{-1}\text{K}^{-1}$  for  $d = 130 \text{ nm}$  nanowire at  $T = 300 \text{ K}$ . This value is almost one

half of the value reported in other bulk polycrystalline samples [4,21], but is roughly the same order of magnitude as  $\kappa$  along the  $a$ -axis [14] (continuous lines are results from calculations in reference [14]). This can be expected as the growth direction of the nanowires was oblique to this axis such that the weak bonding will reduce thermal conductivity similar to if the growth direction was along the  $a$ -axis. The reduction in the measured  $\kappa$  at small diameters may indicate static defects or an underestimation of the contribution of long wavelength phonons in the calculation of Guo et. al.[14] Figure 4.8(b), shows the dependence of  $ZT$  on the diameter at room temperature (290K) in which an overall increase in  $ZT$  is observed by reducing the nanowires diameter. Figure 4.8(b) confirms a significant enhancement of  $ZT$  as the diameter of the nanowire is reduced below 190 nm.

In order to better understand the observed transport response in our SnSe nanowires, density functional theory (DFT) calculations were performed using the Vienna Ab initio simulation package (VASP) [25]. The many-body GW approximation was implemented with the projector augmented wave (PAW) scheme [26] and the generalized gradient approximation of Perdew, Burke and Ernzerhof (GGA-PBE) [27] for the electronic correlation functional. The energy cut-off for the plane wave expansion was 450 eV. The Brillouin zones of the bulk SnSe were sampled in a gamma-centered grid with a k-point mesh of  $5 \times 15 \times 15$ . To obtain an accurate DOS, the  $k$ -point mesh of the non-self-consistent calculation was increased to  $11 \times 33 \times 33$ . Atomic positions and unit cell vectors are relaxed until all the forces and components of the stress tensor are below

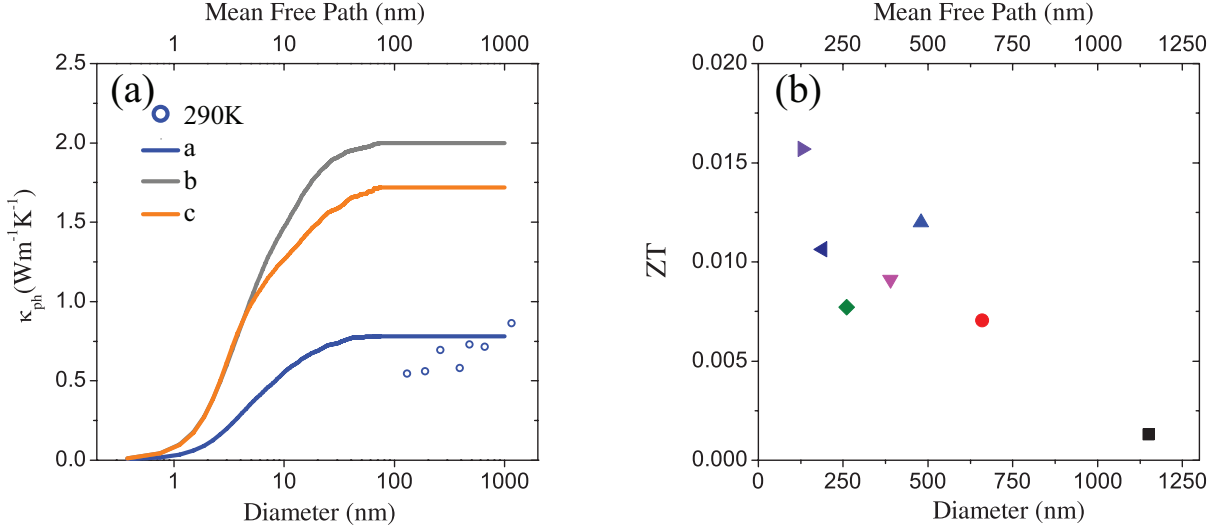


Figure 4.8: (a) Lattice thermal conductivity in comparison with calculated accumulated thermal conductivity data of Guo et. al. [14] in a, b and c directions and (b) figure of merit  $ZT$  at 290 K for different diameters.

0.001 eV Å<sup>-1</sup>. Starting from the experimental orthorhombic structure (space group Pnma 62) with lattice parameter ( $a = 11.46, b = 4.14$  and  $c = 4.38$  Å) the calculated indirect bandgap ( $E_g$ ) was 0.654389 eV, which is smaller than the experimental bandgap [1]. Underestimation of the bandgap is a well-known result in the DFT calculations [28] that does not affect the intended analysis. Figure 4.9 shows the crystal structure (a), the band diagram (b), and density of states (c), for SnSe. These calculations served as input to determine the electronic transport parameters.

The transport properties were calculated based on the Boltzmann transport equation under the rigid band and constant relaxation time approximations as implemented on the BoltzTraP package [29]. This numerical package has been previously used to study SnSe

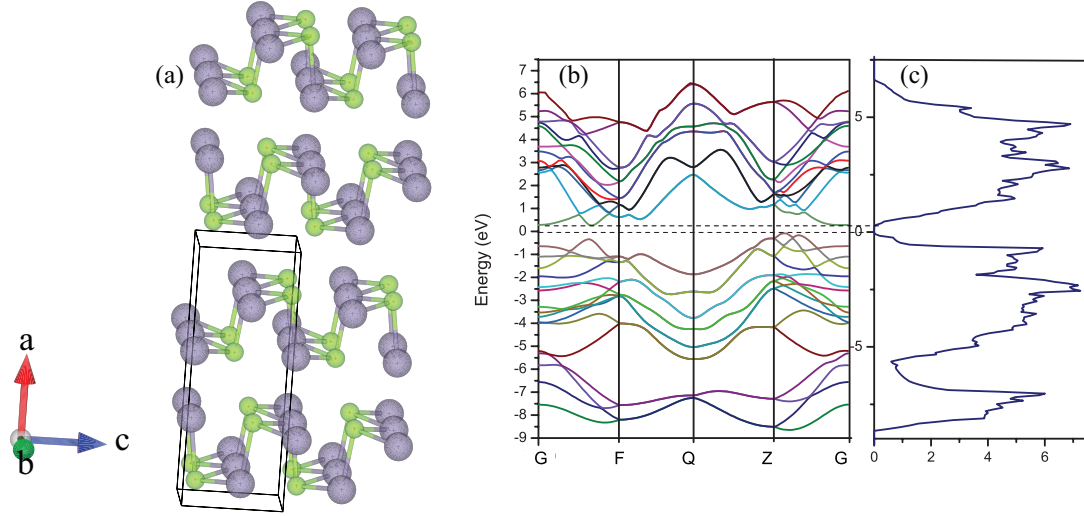


Figure 4.9: (a) Crystal structure of the Pnma phase of SnSe. The primitive cell is shown as a black line. Gray larger balls represent Sn atoms and green smaller balls are Se atoms. (b) The calculated band structure and (c) the total density of states.

materials with good results [5,7,8,10,13,17]. Due to SnSe crystal structure, the transport is anisotropic and averaged values corresponding to the [111] direction are shown. Figure 4.10(a) shows the calculated  $S$  at different temperatures as a function of the chemical potential referenced to the valence band maximum,  $\mu - E_{VBM}$ . By interpolating the experimental data the temperature dependence of  $\mu$  was determined in the samples. Figure 4.10(b) shows an increasing  $\mu$  with temperature with values suggesting a high density of holes that keeps the chemical potential near or in the conduction band at low temperatures.

To confirm these observations, Boltztrap calculations were used to estimate the density of holes of the material. In figure 4.6(a) the calculated  $S(T)$  curve for a density of holes  $p = 1 \times 10^{19} \text{ cm}^{-3}$  is included (figure 4.6(a) solid line) that fits the measured  $S$

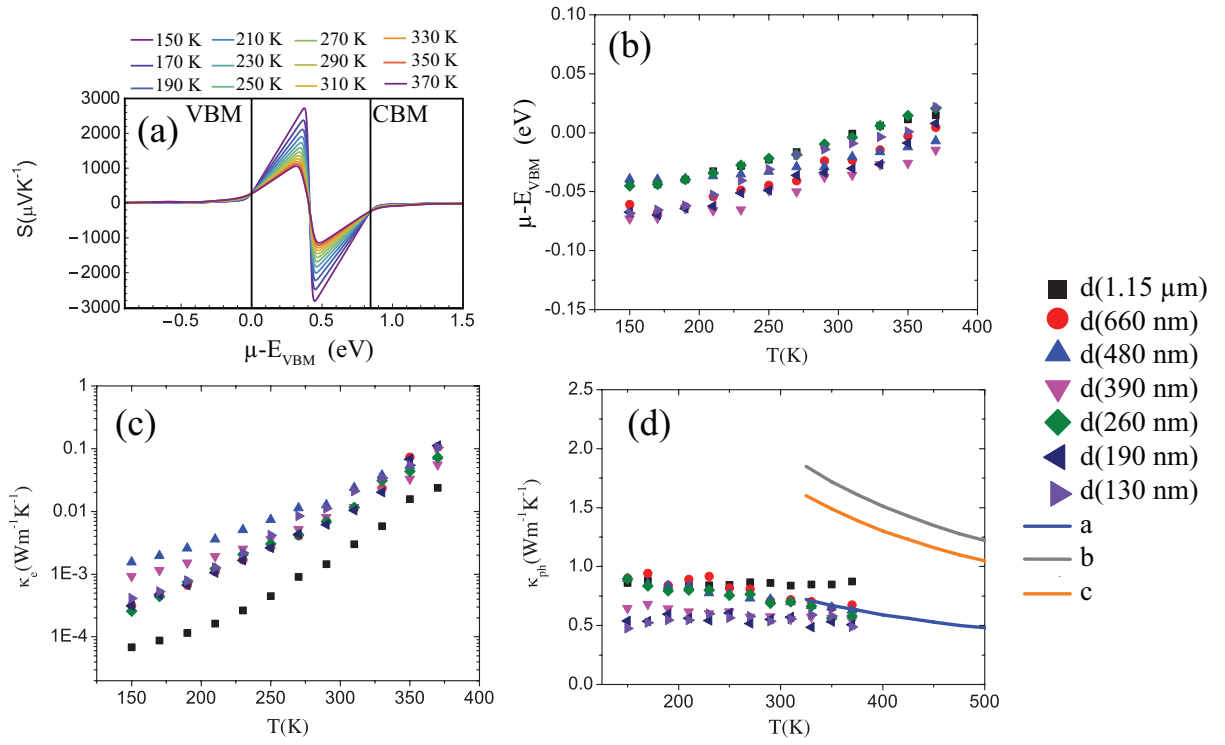


Figure 4.10: The calculated thermoelectric properties of SnSe. (a) Seebeck coefficient as a function of the chemical potential ( $\mu - E_{VBM}$ ), the energy position of the band edges ( $E_{VBM}$  and  $E_{CBM}$ ) is identified by vertical dotted lines. (b) The calculated temperature dependences of the chemical potential ( $\mu - E_{VBM}$ ). (c) The calculated electron ( $\kappa_e$ ) and (d) lattice ( $\kappa_{ph}$ ) thermal conductivities contributions. Calculated  $\kappa_{ph}$  from Guo et. al. [14] is shown in figure (d) with continuous lines in  $a$ ,  $b$  and  $c$  crystal directions.

for the 480 nm nanowire, thus assigning a larger density of vacancies produced during the nanowire formation as compared with other synthesis methods used to grow crystalline and polycrystalline bulk samples [1,4,20,21,24]. The electrical conductivity of the nanowires ( $\sigma \sim 400\text{S/m}$  at  $T = 300\text{K}$ ) is lower than the reported values in high quality SnSe bulk crystals with similar density of holes [5] suggesting a larger density of defects.

As for the thermal transport, the measured thermal conductivity  $\kappa$  includes contributions from phonon and free charges. The calculated values of  $\mu$  were used to determine the contribution of the charge carriers to total. From there, the thermal conductivity due to phonons was obtained by subtraction of the calculated electronic contribution to the measured thermal conductivity, that is to say:  $\kappa_{ph} = \kappa_{total} - \kappa_e$  (figure 4.10(d)). As shown in figures 4.10(c) and 4.10(d), the contribution due to free charges was in some cases up to 2 orders of magnitude lower than the contribution due to phonons therefore, the measured thermal conductivity (Figure 4.6(b)) is dominated by phonon transport (Figure 4.10d) as previously observed in nanowires of other semiconductor materials [3,17]. For comparison, figure 4.10(d) also shows continue lines corresponding to Guo et. al. results [14]. A fitting of the experimental results within the Debye Callaway approximation that considers surface scattering due to reducing diameter while keeping the density of defects constant.

We fitted  $\kappa_{ph}(T)$  using a modified Debye-Callaway model [32], with contributions due to impurities, point defects, umklapp and surface boundary phonon scattering events. In general,  $\kappa_{ph}(T)$  can be expressed as:

$$\kappa_{ph}(T) = \frac{k_B}{2\pi^2 v_s} \left( \frac{k_B T}{\hbar} \right)^3 \int_0^{T_D/T} \frac{x^4 e^x}{\tau_{ph}^{-1} (e^x - 1)^2} dx \quad (4.1)$$

with:

$$\tau_{ph}^{-1} = \tau_I^{-1} + \tau_D^{-1} + \tau_U^{-1} + \tau_B^{-1} + \dots \quad (4.2)$$

$$= A\alpha^4 T^4 x^4 + RTx + B\alpha^2 T^3 x^3 \exp\left(-\frac{T_D}{T}\right) + \frac{v_s}{t} + \dots \quad (4.3)$$

Where  $x = \frac{\hbar\omega}{k_B T}$  is the reduced phonon frequency,  $\hbar$  is the Planck constant,  $k_B$  is the Boltzmann constant,  $v_s = 1746 \text{ m/s}$  is the speed of sound in SnSe,  $T_D = 49K$  is the Debye temperature for SnSe and  $T$  is the absolute temperature. The chosen values for  $v_s$  and  $T_D$  for the [111] growth direction of our samples correspond to the average of the three crystal orientations taken from Zhao et. al. calculations[1]. The fitting parameters are  $A$  for impurities,  $R$  dislocations,  $B$  for umklapp process and  $L$  is the mean free path due to surface boundary scattering. Here we assign  $L$  to the measured diameter of the nanowire. In order to stress the contribution of the phonon surface scattering to the reduction of the thermal conductivity in SnSe nanowires, we maintained constant  $A = 1 \times 10^{-4} \text{ (s}^3\text{)}$ ,  $R = 8 \times 10^8 \text{ (s}^{-1}\text{K}^{-1}\text{)}$ ,  $B = 0.5 \times 10^{-17} \text{ (sK}^{-1}\text{)}$  in all cases and calculated the thermal dependence of  $\kappa_{ph}$  for two diameters:  $L_1 = 130 \text{ nm}$  and  $L_2 = 1.15 \text{ }\mu\text{m}$ .

Figure 4.11, shows an overall match between the fitting from the modified Debye-Callaway model and the experimental data for larger and smaller diameters giving some role to the phonon's surface scattering to the thermal conductivity within the range of diameters used in this study, measuring  $0.55 \text{ Wm}^{-1}\text{K}^{-1}$  at  $T = 300K$  in the  $d = 130 \text{ nm}$



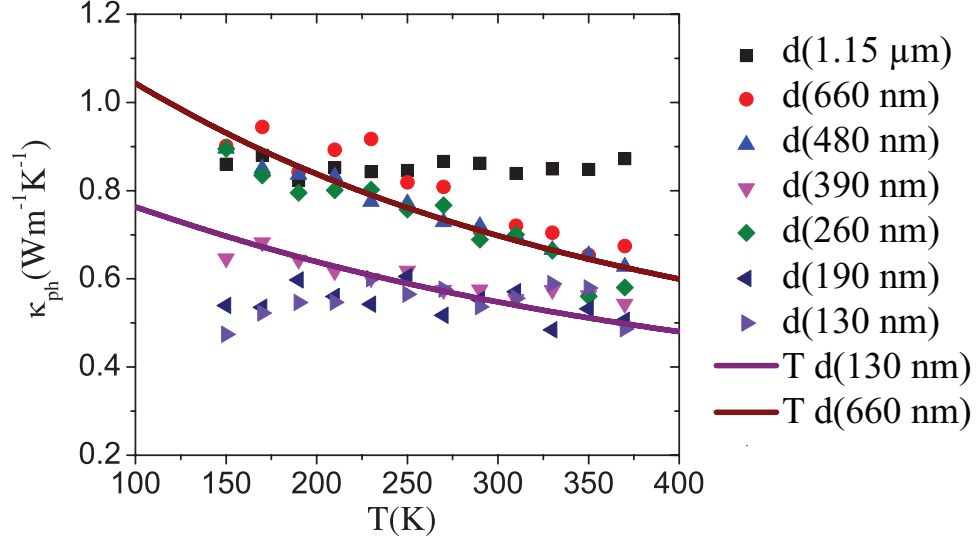


Figure 4.11: The measured lattice thermal conductivities ( $\kappa_{ph}$ ) for each nanowire. The calculated  $\kappa_{ph}$  for two diameters ( $L_1$  and  $L_2$ ) are shown with continuous lines.

nanowire. Multilayered materials with layer thickness  $\sim 30$  nm reported lower thermal conductivities [21] that anticipates a further reduction of  $\kappa$  in nanowires with lower diameters.

**Why Bulk calculations?** We used bulk parameters for the calculations because the diameters of the measured nanowires are greater than 100 nm and our calculations show bulk-like electron energy states configuration in nanowires with diameters above 10 nm (see figure 4.12). Using the Vienna ab-initio simulation package (VASP), projected density of states calculation was performed to demonstrate that surface electron states in a 100 nm SnSe sample contribute less than  $\sim 1\%$  of the total states. A (1 1 1) slab was analyzed in the orthorhombic structure of the SnSe crystal, holding a total of 18 layers and 5nm thick slab. As in the main work, a many-body GW approximation was

implemented with the projector augmented wave (PAW) scheme, and the generalized gradient approximation of Perdew, Burke and Ernzerhof (GGA-PBE) for the electronic correlation functional. A gamma centered grid with k-point meshes of  $3 \times 9 \times 1$  and a cutoff energy of 450 eV was chosen for the self-consistent calculation. The k-point mesh was increased to  $5 \times 15 \times 1$  for the non-self-consistent calculation holding the same cut off energy.

The contribution of states per layer is presented in the projected density of states calculation (Fig 4.12). Results clearly demonstrate the little share that surface states present in the inner 4<sup>th</sup> to 14<sup>th</sup> layers that already resemble the bulk density of states. The synthesized nanowires have diameters larger than 100 nm, then these results justify the use of 3D periodic Density of States configuration to calculate the electron energies of the measured SnSe nanowires.

## 4.3 Summary

The VLS synthesis of SnSe nanowires and the successful measurement of the Seebeck coefficient and the thermal and electrical conductivities of individual nanowires with diameters from  $\sim 130$  nm to  $\sim 1.15$   $\mu\text{m}$ , over a 150-370 K temperature range is reported. HRTEM and XRD analyses confirm large crystalline grain size and growth along the [111] direction. The thermoelectrical measurements were carried out with suspended specialized four-probe micro-thermometry devices. All measurements were consistent

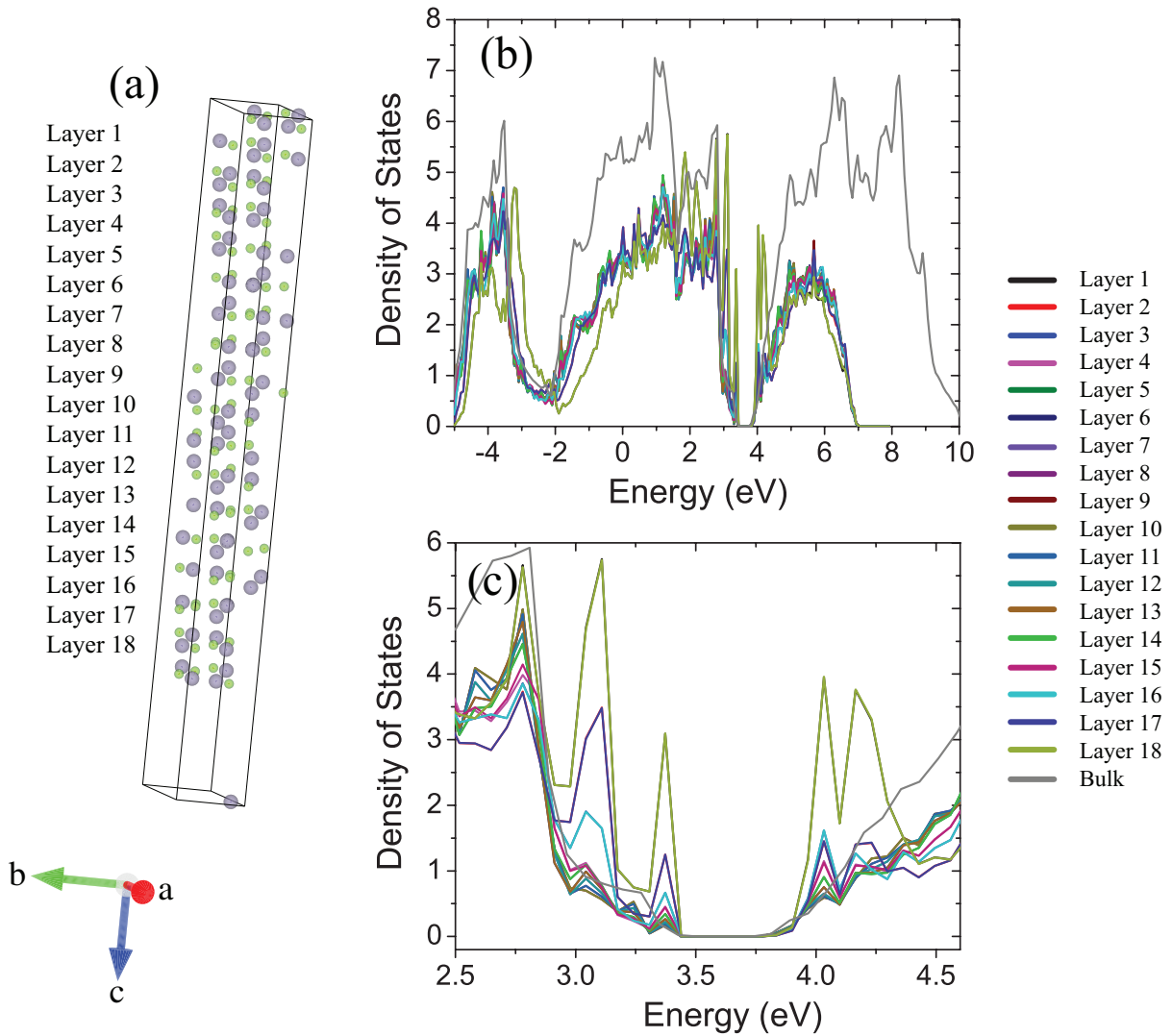


Figure 4.12: (a) Supercell Crystal structure of the low temperature Pnma phase SnSe with 18 layers. Gray balls are Sn atoms and green are Se atoms. (b) Calculated Density of States per layer as a function of the chemical potential for modeled nanowire with 5 nm in diameter (c) is the same as (b) with different scales.

with previous publications for the material in bulk, but a clear reduction of the thermal

conductivity and a clear increase in  $ZT$  is observed with decreasing nanowire diameter. We observed no significant dependence of the thermopower on the diameter of the nanowires within the studied range. Theoretical band structure and transport model calculations were used to correlate free charges parameters with measured data. The chemical potential values confirm high  $p$ -type doping in all cases with a hole density in the order of  $\sim 1 \times 10^{19} \text{ cm}^{-3}$ . The electrical conductivity is thermally activated as reported in bulk samples and attributed to changes in the density of holes and increasing hole mobility due to charged defects. The measured thermal conductivity in thicker nanowires is consistent with bulk data and the decrease of  $\kappa_{ph}$  with decreasing diameters is consistent with the corresponding increase of the phonon-surface scattering and may indicate an underestimation by previous theoretical models of the contribution of long wavelength phonons to the lattice thermal conductivity in SnSe or an increasing density of defects in thinner nanowires. A maximum  $ZT$  of 0.156 at  $T = 370\text{K}$  was determined for the thinner nanowire that encourages the synthesis of nanowires with lower diameters that can be used as building blocks for high  $ZT$  nanodevices operating near room temperature.

## 4.4 References

- [1] Zhao, L.-D.; Lo, S.-H.; Zhang, Y.; Sun, H.; Tan, G.; Uher, C.; Wolverton, C.; Dravid, V. P.; Kanatzidis, M. G. *Nature* 2014, 508, (7496), 373-377.
- [2] Carrete, J.; Mingo, N.; Curtarolo, S. *Applied Physics Letters* 2014, 105, (10), 101907.
- [3] Li, C.; Hong, J.; May, A.; Bansal, D.; Chi, S.; Hong, T.; Ehlers, G.; Delaire, O. *Nature Physics* 2015, 11, (12), 1063.
- [4] Chen, C.-L.; Wang, H.; Chen, Y.-Y.; Day, T.; Snyder, G. J. *Journal of Materials Chemistry A* 2014, 2, (29), 11171-11176.
- [5] Zhao, L.-D.; Tan, G.; Hao, S.; He, J.; Pei, Y.; Chi, H.; Wang, H.; Gong, S.; Xu, H.; Dravid, V. P. *Science* 2015, 3749.
- [6] Singh, N. K.; Bathula, S.; Gahtori, B.; Tyagi, K.; Haranath, D.; Dhar, A. *Journal of Alloys and Compounds* 2016, 668, 152-158.
- [7] Ding, G.; Gao, G. *Materials Science* 2015, (v1).
- [8] Guan, X.; Lu, P.; Wu, L.; Han, L.; Liu, G.; Song, Y.; Wang, S. *Journal of Alloys and Compounds* 2015, 643, 116-120.
- [9] Kutorasinski, K.; Wiendlocha, B.; Kaprzyk, S.; Tobola, J. *Physical Review B* 2015, 91, (20), 205201.

- 
- [10] Shi, G.; Kioupakis, E. *Journal of Applied Physics* 2015, 117, (6), 065103.
  - [11] Suzuki, Y.; Nakamura, H. *Physical Chemistry Chemical Physics* 2015, 17, (44), 29647-29654.
  - [12] Wang, Z.; Wang, J.; Zang, Y.; Zhang, Q.; Shi, J. A.; Jiang, T.; Gong, Y.; Song, C. L.; Ji, S. H.; Wang, L. L. *Advanced Materials* 2015, 27, (28), 4150-4154.
  - [13] Wang, F. Q.; Zhang, S.; Yu, J.; Wang, Q. *Nanoscale* 2015, 7, (38), 15962-15970.
  - [14] Guo, R.; Wang, X.; Kuang, Y.; Huang, B. *Physical Review B* 2015, 92, (11), 115202.
  - [15] Butt, F. K.; Mirza, M.; Cao, C.; Idrees, F.; Tahir, M.; Safdar, M.; Ali, Z.; Tanveer, M.; Aslam, I. *CrystEngComm* 2014, 16, (17), 3470-3473.
  - [16] Shi, L.; Li, D.; Yu, C.; Jang, W.; Kim, D.; Yao, Z.; Kim, P.; Majumdar, A. *Journal of heat transfer* 2003, 125, (5), 881-888.
  - [17] Mavrokefalos, A.; Pettes, M. T.; Zhou, F.; Shi, L. *Review of scientific instruments* 2007, 78, (3), 034901.
  - [18] Pettes, M. T.; Shi, L. *Advanced Functional Materials* 2009, 19, (24), 3918-3925.
  - [19] Valentín, L.; Betancourt, J.; Fonseca, L.; Pettes, M.; Shi, L.; Soszyński, M.; Huczko, A. *Journal of Applied Physics* 2013, 114, (18), 184301.
  - [20] Sassi, S.; Candolfi, C.; Vaney, J.-B.; Ohorodniichuk, V.; Masschelein, P.; Dauscher, A.; Lenoir, B. *Applied Physics Letters* 2014, 104, (21), 212105.

- 
- [21] Serrano-Sánchez, F.; Gharsallah, M.; Nemes, N.; Mompean, F.; Martinez, J.; Alonso, J. Applied Physics Letters 2015, 106, (8), 083902.
  - [22] Prasher, R. Applied Physics Letters 2009, 94, (4), 041905.
  - [23] Chen, R.; Hochbaum, A. I.; Murphy, P.; Moore, J.; Yang, P.; Majumdar, A. Physical review letters 2008, 101, (10), 105501.
  - [24] Martin, P.; Aksamija, Z.; Pop, E.; Ravaioli, U. Physical review letters 2009, 102, (12), 125503.
  - [25] Chen, S.; Cai, K.; Zhao, W. Physica B: Condensed Matter 2012, 407, (21), 4154-4159.
  - [26] Kresse, G.; Furthmüller, J. Computational Materials Science 1996, 6, (1), 15-50.
  - [27] Blöchl, P. E. Physical Review B 1994, 50, (24), 17953.
  - [28] Perdew, J. P.; Burke, K.; Ernzerhof, M. Physical review letters 1996, 77, (18), 3865.
  - [29] Sham, L.; Schlüter, M. Physical Review Letters 1983, 51, (20), 1888.
  - [30] Madsen, G. K.; Singh, D. J. Computer Physics Communications 2006, 175, (1), 67-71.
  - [31] Ding, G.; Gao, G.; Yao, K. scientific reports 2015, 5, 9567
  - [32] Callaway, J., Model for lattice thermal conductivity at low temperatures. Physical Review, **1959**. 113(4): p. 1046.

# Chapter 5

## Thermoelectric Properties of $\text{Sb}_2\text{Se}_3$ Hexagonal Nanotubes

---

### 5.1 Introduction

Antimony Selenide  $\text{Sb}_2\text{Se}_3$  is a semiconductor with an orthorhombic crystal structure. The main application of  $\text{Sb}_2\text{Se}_3$  is related to switching effects [1], photovoltaic [2] and thermoelectrics [3] properties.  $\text{Sb}_2\text{Se}_3$  nanostructures have been grown using different methods: gas induced reduction, CVD, PLD and many others [4-9].  $\text{Sb}_2\text{Se}_3$  exhibits high Seebeck coefficient but low electrical conductivity in bulk samples however, though the low-dimension fabrication the electrical conductivity has been increased up 3-4 orders of magnitude in whiskers [10] and nanotubes [11] and up 10 order of magnitude in nanowires [11]. At the same time, the growth of the material at the nanoscale size increases the surface-to-volume ratio and may take advantage of the scattering of phonons at the surface boundaries to reduce the thermal conductivity, thus possibly bringing increasing energy conversion efficiency. The interest in this work is then on the fabrication



and study of nanostructured  $\text{Sb}_2\text{Se}_3$  hexagonal nanotubes (HNT), using specialized suspended microtermometer devices to simultaneously measure  $S$ ,  $\sigma$  and  $\kappa$  with a four-points configuration.

## 5.2 Experimental Results and Discussion

$\text{Sb}_2\text{Te}_3$  HNT were synthesized by chemical vapor deposition (CVD) technique, via vapor liquid solid (VLS) process in a 12-in. horizontal furnace equipped with a 2 in diameter quartz tube. The synthesis was made at atmospheric pressure using a high purity 100 sccm Ar gas as the gas carrier and Sb (Alpha Aesar 99.998%) Se (Alpha Aesar 99.99%) powders as precursors. The temperature was increased to 550 °C on the precursors zone and many silicon substrates coating with a 1-3 nm Au thin film were placed 5 - 15 cm downstream from the hot zone. After 5 hours system the was cooled down naturally, keeping the Ar flow.

$\text{Sb}_2\text{Te}_3$  HNT grew up in large areas as shown in figures 5.1 and 5.2(a). The as synthesized HNT were removed directly from the substrate by micromanipulation and aligned onto the measuring micro-device. Two HNT with 650 and 350 nm in diameter were selected. The electrical contacts between the HNT and the Pt measuring electrodes were improved by depositing Pt at the sample-electrode contact zones using a Focus Ion Beam (FIB).

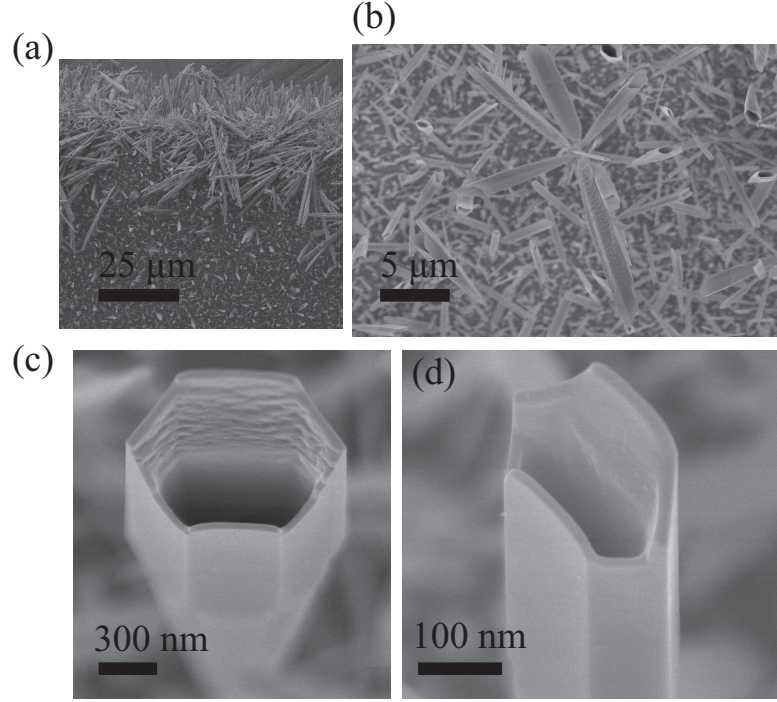


Figure 5.1: SEM images of  $\text{Sb}_2\text{Se}_3$  nanotubes on substrate (a) and (b) shows a different magnification of as grown HNT. (c) and (d) show the hexagonal nanotube morphology of the samples.

Each of the measured samples were analyzed with electron microscopy. Figure 5.2(c) shows the SEM-EDS mapping of one representative measured sample, showing its elemental composition. EDS approximated quantification signal can be correlated with the stoichiometric ratio of Sb:Se 2:3. See figure 5.3 for quantification values and SEM images of the two measured samples on the micro-devices.

The XRD pattern in figure 5.4(c) confirms that  $\text{Sb}_2\text{Se}_3$  HNT has an orthorhombic crystal structure and shows all the index peaks related to  $\text{Sb}_2\text{Se}_3$  (JCPDS 890821) with  $a = 11.401$ ,  $b = 11.943$  and  $c = 3.972$  Å. These values were confirmed with SAED data

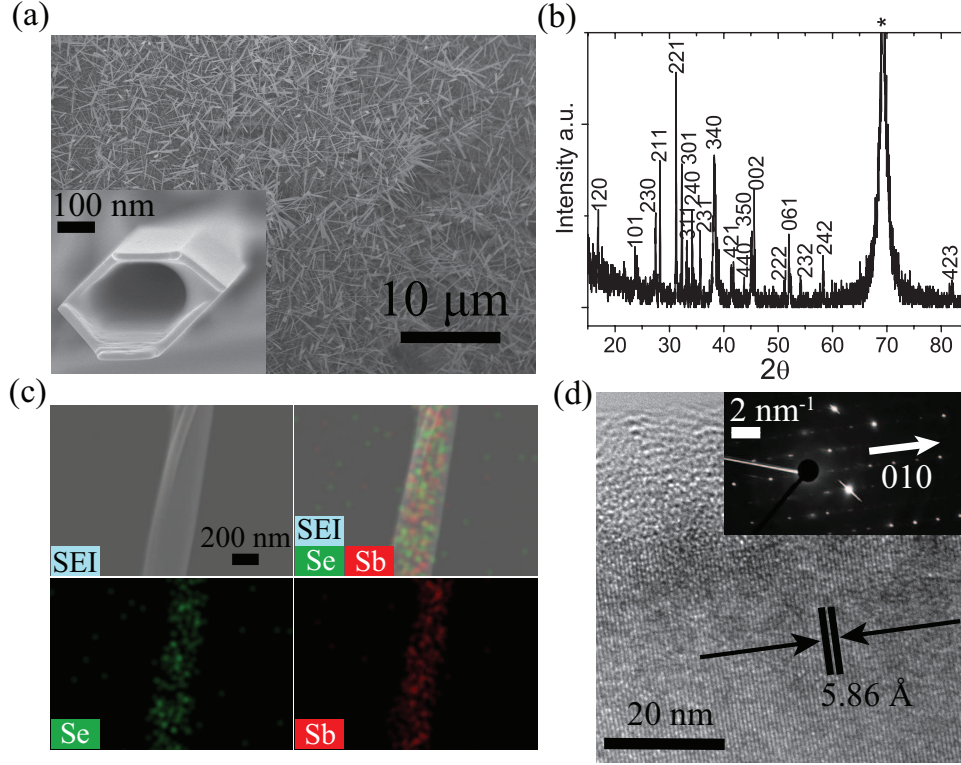


Figure 5.2: a) SEM image of  $\text{Sb}_2\text{Se}_3$  hexagonal as grown nanotubes on the substrate. (b) XRD pattern of as grown material on the substrate. (c) SEM image and SEM-EDS mapping of Sb and Se signals. (d) HRTEM image, insert: SAED.

and HR-TEM image (figure 5.2(d)) of the  $\text{Sb}_2\text{Se}_3$  HNT sample 1.

The measured Seebeck coefficient ( $S$ ) as a function of temperature is displayed in figure 5.4(a) for the two analyzed samples. In both cases  $S$  is positive, revealing that the  $\text{Sb}_2\text{Se}_3$  HNT have  $p$ -type electrical behavior.  $S$  values increase with increasing temperature and consistent with previous reports for this material [10,12,13]. Figure 5.4(a) shows the Seebeck coefficient for  $\text{Sb}_2\text{Se}_3$  HNT as compared with bulk calculations reported by Jayaraman et. al. [14] for a hole-concentration in the order of  $1 \times 10^{19} \text{ cm}^{-3}$ .

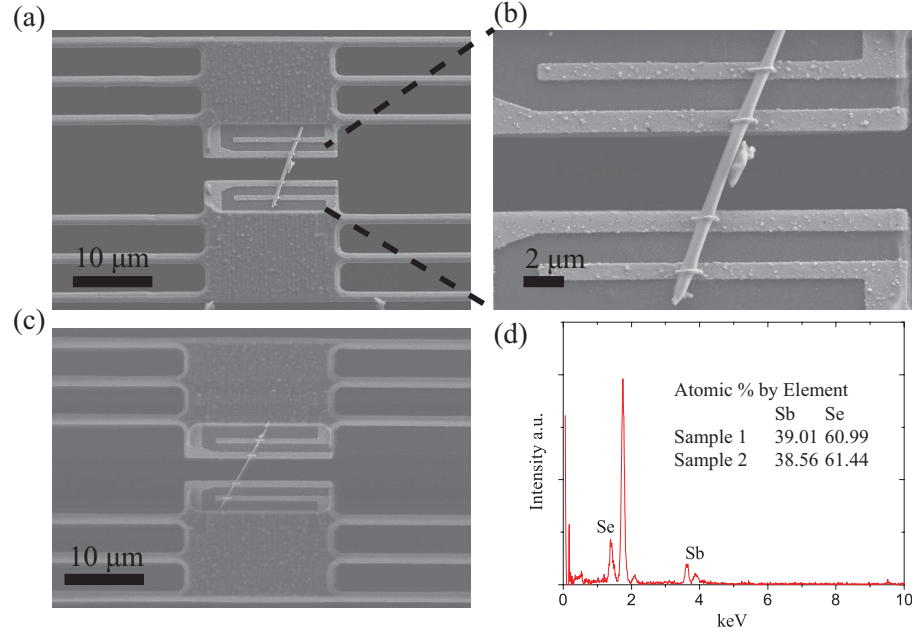


Figure 5.3: SEM images of measured  $\text{Sb}_2\text{Se}_3$  hexagonal nanotubes aligned on specialized suspended micro devices, (a) and (b) different magnification images of sample 1. (c) SEM image of sample 2 and (d) SEM-EDS spectra and atomic percentages of elements found in the measured samples.

Figure 5.4(c) shows the variations in the electrical conductivity depending on temperature. The electrical conductivity in  $\text{Sb}_2\text{Se}_3$  HNT is observed to be thermal activated with and increases with the increase of the temperature. The measured electrical conductivity in  $\text{Sb}_2\text{Se}_3$  HNT are 4-orders of magnitude larger than the  $\text{Sb}_2\text{Se}_3$  bulk values [15] and the reported ones in microtubes [16]. Mehta et al. [11] found high electrical conductivity in  $\text{Sb}_2\text{Se}_3$  nanowires ( $\sim 3 \times 10^4$  S/m) and nanotubes ( $3.5 \times 10^2$  S/m) and in the same order magnitude of the ones here reported. Recently Ko et. al [13] synthesized high and low electrical conductivity nanowires of  $\text{Sb}_2\text{Se}_3$  with conductivities of  $\sim 3 \times 10^4$  S/m and  $4.3 \times 10^{-4}$  S/m, showing a strong coupling between the electrical properties, the

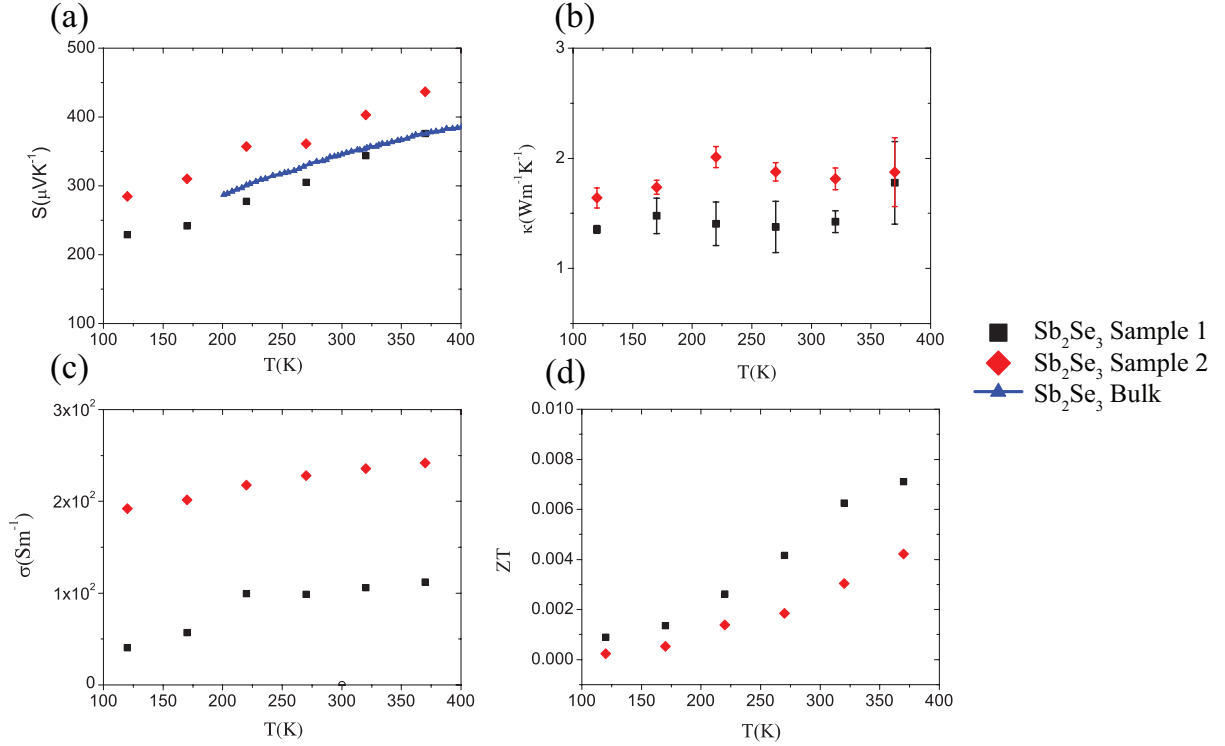


Figure 5.4: (a) Measured Seebeck coefficient  $S$  for the two samples as compared with Bulk calculations [14]. (b) total thermal conductivity  $\kappa$  of the HNT with the error bars. (c) Electrical conductivity of the measured samples. (d) calculated figure of merit  $ZT$  for the samples as a function of temperature.

shape, the crystal structure and the growth conditions of the material. The  $\text{Sb}_2\text{Se}_3$  samples here reported show electrical conductivities in the same order of magnitude of some reported whiskers [10] and nanotubes [11], one order or magnitude larger than reported thin films [17], and 2—orders of magnitude smaller than measured nanowires [11].

Figure 5.4(b) shows the temperature dependence of the thermal conductivity ( $\kappa$ ) for all samples. The thermal conductivity remains practically constant with a slight tendency to increase with temperature, and with values between 1.3 to 1.8  $\text{W m}^{-1} \text{K}^{-1}$ . These values

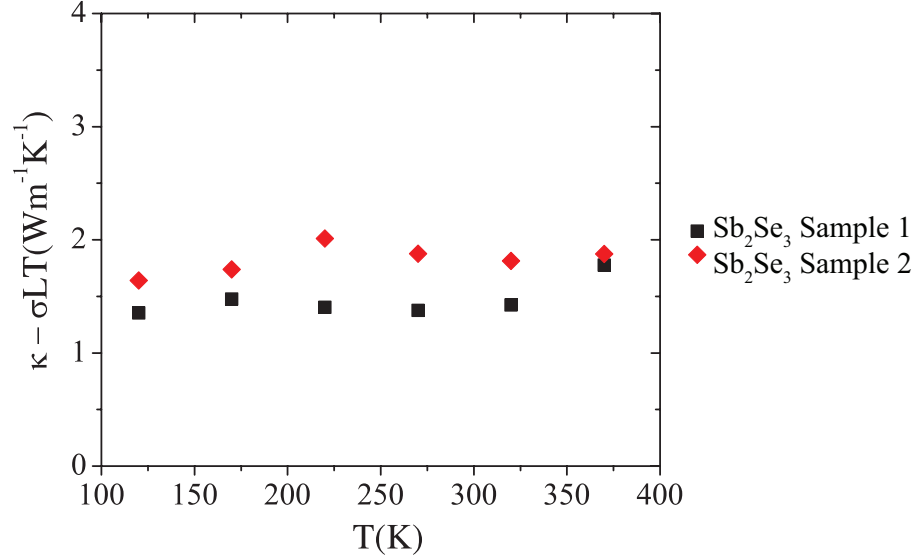


Figure 5.5: Calculate lattice thermal conductivity for the measured samples as a function of temperature.

are half of the ones reported in bulk samples [15] and of the same order of magnitude than those reported in nanowires and nanotubes [11,13]. The lattice contribution to the thermal conductivity was calculated using the approximation:  $\kappa_L = \kappa_{Total} - \sigma LT$  and  $L = (1.5 + \exp(-|S|/116)) \times 10^{-8} \text{ W}\Omega\text{K}^{-2}$ , applicable to non-degenerated semiconductors, obtaining values between  $1.64 - 1.52 \times 10^{-8} \text{ W}\Omega\text{K}^{-2}$ . Figure 5.5 shows that the main contribution to the observed thermal conductivity comes from lattice vibrations in the HNT samples.

Finally, the figure of merit  $ZT$  was calculated and shown in figure 5.4(d) for all the measured samples. The calculated  $ZT$  values show a maximum of  $\sim 0.0071$  at 370K, 4–order of magnitude larger than the reported bulk values. In all the samples the values for  $ZT$  increased with the increase of temperature. These results show that  $\text{Sb}_2\text{Se}_3$

HNTs considerably improve the figure of merit due to the increase of their electrical conductivity. This result makes such morphology a preferred one in this material for future thermoelectric room temperature applications.

### 5.3 Summary

We successfully measured the Seebeck coefficient, the thermal and the electrical conductivities of individual  $\text{Sb}_2\text{Se}_3$  HNTs over a 120-370 K temperature range. HNTs were synthesized by CVD and the measurements were carried out using specialized suspended four-probe microdevices in high vacuum. The thermopower  $S$  has a positive value and increase with temperature in all samples. Electrical conductivity behavior suggests a thermal activated behavior and was 4 orders of magnitude larger than those reported in bulk samples. The significant increase in the electrical conductivity is recognized as the cause of the enhanced ZT values obtained in HNTs samples.

## 5.4 References

- [1] Platakis, N. and H. Gatos, Threshold and memory switching in crystalline chalcogenide materials. *physica status solidi (a)*, 1972. 13(1): p. K1-K4.
- [2] Rajpure, K., C. Lokhande, and C. Bhosale, Effect of the substrate temperature on the properties of spray deposited Sb<sub>2</sub>Se<sub>3</sub> thin films from non-aqueous medium. *Thin Solid Films*, 1997. 311(1-2): p. 114-118.
- [3] Black, J., et al., Electrical and optical properties of some M<sub>2</sub>N<sub>3</sub> b semiconductors. *Journal of Physics and Chemistry of Solids*, 1957. 2(3): p. 240-251.
- [4] Zhai, T., et al., Recent Developments in One-Dimensional Inorganic Nanostructures for Photodetectors. *Advanced Functional Materials*, 2010. 20(24): p. 4233-4248.
- [5] Ma, J., et al., One-dimensional Sb<sub>2</sub>Se<sub>3</sub> nanostructures: solvothermal synthesis, growth mechanism, optical and electrochemical properties. *CrystEngComm*, 2011. 13(7): p. 2369-2374.
- [6] Ma, J., et al., Controlled synthesis of one-dimensional Sb<sub>2</sub>Se<sub>3</sub> nanostructures and their electrochemical properties. *The Journal of Physical Chemistry C*, 2009. 113(31): p. 13588-13592.



- 
- [7] Choi, D., et al., Diameter-controlled and surface-modified Sb<sub>2</sub>Se<sub>3</sub> nanowires and their photodetector performance. *Scientific reports*, 2014. 4: p. 6714.
- [8] Zhai, T., et al., Single-Crystalline Sb<sub>2</sub>Se<sub>3</sub> Nanowires for High-Performance Field Emitters and Photodetectors. *Advanced Materials*, 2010. 22(40): p. 4530-4533.
- [9] Ota, J. and S.K. Srivastava, Synthesis and optical properties of Sb<sub>2</sub>Se<sub>3</sub> nanorods. *Optical Materials*, 2010. 32(11): p. 1488-1492.
- [10] Wu, H.-j., et al., Self-assisted nucleation and growth of [010]-oriented Sb<sub>2</sub>Se<sub>3</sub> whiskers: the crystal structure and thermoelectric properties. *Journal of Materials Chemistry C*, 2015. 3(40): p. 10488-10493.
- [11] Mehta, R.J., et al., High electrical conductivity antimony selenide nanocrystals and assemblies. *Nano letters*, 2010. 10(11): p. 4417-4422.
- [12] Chakraborty, B., et al., Magnetic and electric properties of antimony selenide (Sb<sub>2</sub>Se<sub>3</sub>) crystals. *Journal of Physics and Chemistry of Solids*, 1980. 41(8): p. 913-917.
- [13] Ko, T.-Y., M. Shellaiah, and K.W. Sun, Thermal and thermoelectric transport in highly resistive single Sb<sub>2</sub>Se<sub>3</sub> nanowires and nanowire bundles. *Scientific reports*, 2016. 6: p. 35086.

- 
- [14] Jayaraman, A., A. Bhat Kademane, and M. Molli, DFT study on the carrier concentration and temperature-dependent thermoelectric properties of antimony selenide. *Indian Journal of Materials Science*, 2016. 2016.
- [15] Gribnyak, L. and T. Ivanova, Electrical properties of single crystal antimony selenide. *Inorg. Mater.(Engl. Transl.);(United States)*, 1987. 23(4).
- [16] Zheng, X., et al., Growth of  $\text{Sb}_2\text{E}_3$  ( $\text{E} = \text{S}, \text{Se}$ ) polygonal tubular crystals via a novel solvent-relief-self-seeding process. *Inorganic chemistry*, 2002. 41(3): p. 455-461.
- [17] Wang, X., et al., Preparation and electrical transport properties of nanostructured  $\text{Sb}_2\text{Se}_3$  films fabricated by combining spin-coating and gas-induced reduction. *Journal of nanoparticle research*, 2013. 15(4): p. 1541.

# Chapter 6

## Concluding Remarks and Future Recommendations

---

### 6.1 Conclusions

We successfully measured the Seebeck coefficient, and the thermal and electrical conductivities to obtain the thermoelectric figure of merit of individual single crystalline ITO nanowires, with and without 30 minutes of thermal treatment in air at temperatures up to 1300°C. ITO nanowires were synthesized by a VLS process with diameters in the 180-330 nm range. The comparison between the samples' response with and without annealing showed relatively high thermal tolerance of the material at the nanoscale that encourages its use in applications designed to operate at high temperatures up to 1300°C. In particular, the thermoelectric response of the studied ITO nanowires makes them a promising candidate as  $n$ -type thermoelectric building block to develop nanodevices to operate in harsh environments.

We reported the VLS synthesis of SnSe nanowires and successfully measured the Seebeck coefficient and the thermal and electrical conductivities of individual nanowires with

diameters from  $\sim 130$  nm to  $\sim 1.15$   $\mu\text{m}$ , over a 150-370 K temperature range. HRTEM and XRD analyses confirm large crystalline grain size and growth along the [111] direction. The thermoelectrical measurements were carried out with suspended specialized four-probe micro-thermometry devices. All measurements were consistent with previous publications for the material in bulk, but a clear reduction of the thermal conductivity and a clear increase in  $ZT$  is observed with decreasing nanowire diameter. We observed no significant dependence of the thermopower on the diameter of the nanowires within the studied range. Theoretical band structure and transport model calculations were used to correlate free charges parameters with measured data. The chemical potential values confirm high  $p$ -type doping in all cases with a hole density in the order of  $\sim 1 \times 10^{19}$   $\text{cm}^{-3}$ . The electrical conductivity is thermally activated as reported in bulk samples and attributed to changes in the density of holes and increasing hole mobility due to charged defects. The measured thermal conductivity in thicker nanowires is consistent with bulk data and the decrease of  $\kappa_{ph}$  with decreasing diameters is consistent with the corresponding increase of the phonon-surface scattering and may indicate an underestimation by previous theoretical models of the contribution of long wavelength phonons to the lattice thermal conductivity in SnSe or an increasing density of defects in thinner nanowires. A maximum  $ZT$  of 0.156 at  $T = 370\text{K}$  was determined for the thinnest nanowire that encourages the synthesis of nanowires with smaller diameters that can be used as building blocks for high  $ZT$  nanodevices operating near room temperature.

We successfully measured the Seebeck coefficient, and the thermal and electrical conductivities of individual  $\text{Sb}_2\text{Se}_3$  HNT over a 120-370 K temperature range. The HNT were synthesized by CVD and the measurements were carried out using specialized suspended four-probe microdevices in high vacuum. The thermopower  $S$  has a positive value and increases with temperature in all samples. Electrical conductivity measurements suggest a thermally activated behavior in HNT. The electrical response in measured HNT is 4 orders of magnitude larger than the reports for bulk samples.

## 6.2 Future Recommendations

- Through the research work carried out for this thesis, we have developed an approach to synthesize nanowires with promising thermoelectric applications, as well as micro-manipulation techniques for nanowires with diameters above 80nm. However, to manipulate thinner samples the to access a double column FIB (electron-ion column) equipped with in situ micro-manipulators.
- More studies with TEM-SAED, EELS and HR-Raman of these nanostructure over the studied temperature range is suggested.
- The implementation of experimental routines for surface functionalization, the reduction of the nanowires diameters, controlled doping, nanodecorations, and others in different nanowires materials is also suggested in order to increase the thermoelectric efficiency. Finally, to explore the Spin-Seebeck effect as a novel approach to

---

increase ZT is recommendable.